



# Silica–Ceria sandwiched Ni core–shell catalyst for low temperature dry reforming of biogas: Coke resistance and mechanistic insights

S. Das<sup>a</sup>, J. Ashok<sup>a</sup>, Z. Bian<sup>a</sup>, N. Dewangan<sup>a</sup>, M.H. Wai<sup>a</sup>, Y. Du<sup>b</sup>, A. Borgna<sup>b</sup>, K. Hidajat<sup>a</sup>, S. Kawi<sup>a,\*</sup>

<sup>a</sup> Department of Chemical and Biomolecular Engineering, National University of Singapore, Singapore 119260, Singapore

<sup>b</sup> Institute of Chemical and Engineering Sciences, A\*STAR, 1 Pesek Road, Jurong Island, 627833, Singapore

## ARTICLE INFO

### Keywords:

Dry reforming of methane  
Coke resistance  
DRIFTS

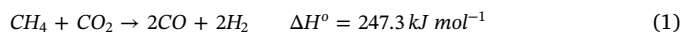
## ABSTRACT

In this paper, a novel sandwiched core–shell structured Ni-SiO<sub>2</sub>@CeO<sub>2</sub> catalyst, with nickel nanoparticles encapsulated between silica and ceria, was developed and applied for dry reforming of biogas (CH<sub>4</sub> / CO<sub>2</sub> = 3/2) under low temperature conditions to test its coke inhibition properties. Ni-phyllsilicate was used as the Ni precursor in order to produce highly dispersed Ni nanoparticles on SiO<sub>2</sub>. Cerium oxide was chosen as the shell due to its high redox potential and oxygen storage capacity, that can reduce coke formation under severe dry reforming conditions. The core shell Ni-SiO<sub>2</sub>@CeO<sub>2</sub> catalyst showed excellent coke inhibition property under low temperature (600 °C) reforming of biogas, with no coke detected after a 72 h catalytic run. Under the same conditions, Ni-SiO<sub>2</sub> catalyst deactivated within 22 h due to heavy coke formation and reactor blockage, while Ni-CeO<sub>2</sub> catalyst showed very low activity. The higher activity of the core–shell catalyst is attributed to its higher Ni dispersion and reducibility. TEM and XRD results show that the core–shell catalyst shows higher resistance to Ni particle sintering and agglomeration during the reaction than the Ni-SiO<sub>2</sub> and Ni-CeO<sub>2</sub> catalysts. *In-situ* DRIFTS on the Ni-SiO<sub>2</sub>@CeO<sub>2</sub> catalyst indicate a change in the reaction mechanism from a mono-functional pathway on the Ni-SiO<sub>2</sub> catalysts to a bi-functional route on the Ni-SiO<sub>2</sub>@CeO<sub>2</sub> catalyst with active participation of oxygen species from CeO<sub>2</sub> in carbon gasification. The confinement effect of the sandwich structure and the bifunctional mechanism of dry reforming are the primary reasons for the excellent coke resistance of the Ni-SiO<sub>2</sub>@CeO<sub>2</sub> catalyst.

## 1. Introduction

With the changing energy landscape and increasing concerns over climate change and global warming, there is increasing focus on developing a hydrogen economy for sustainable development. While clean hydrogen generation by water splitting still remains highly energy intensive and uneconomical, methane containing gaseous fuels such as natural gas, shale gas or bio-gas are currently more economical sources for hydrogen production. Dry reforming of methane using CO<sub>2</sub> as a soft oxidant Eq. (1) to produce syn-gas, a mixture of H<sub>2</sub> and CO, has garnered significant research interest over the last decade due to its economic and environmental benefits. Dry reforming provides a way of consuming two major greenhouse gases, namely CO<sub>2</sub> and CH<sub>4</sub> to produce syn-gas which can be used as a source of hydrogen for fuel cells, as fuel for gas engines or even for producing valuable chemicals through Fischer Tropsch synthesis. Bio-gas is a clean and renewable fuel with CH<sub>4</sub> and CO<sub>2</sub> as the major components and hence is an excellent candidate for dry reforming applications. Bio-gas by itself is a poor quality fuel due to its high CO<sub>2</sub> content that reduces its calorific value and

limits application in combustion engines. Dry reforming of bio-gas obviates the need of separating CO<sub>2</sub> from the bio-gas, and increases its calorific value by converting it to syn-gas.



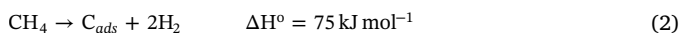
In spite of all the benefits of dry reforming applications, a major hurdle in this process is the development of stable catalysts which are not easily deactivated. The major reason behind the deactivation of the catalyst is deposition of coke or inactive carbonaceous species that can block active sites or plug reactors, thus reducing the useful life of catalyst. Generally, noble metals like Pt, Ru, Ir, Rh and transition metals like Ni, Cu, Co, Fe are active for dry reforming of methane [1,2]. Being cheaper, nickel based catalysts are more economically attractive than noble metal catalysts. However, nickel catalysts have a very high propensity for the formation of coke under dry reforming conditions, which limits their long-term application. Apart from the choice of metal, other factors which contribute towards the abundance of coke deposition over the catalyst are the catalyst structure and composition combined with the reaction conditions. Several studies have shown that coke

\* Corresponding author.

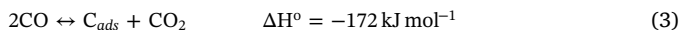
E-mail address: [chekawis@nus.edu.sg](mailto:chekawis@nus.edu.sg) (S. Kawi).

formation is reduced at high reaction temperatures ( $> 800\text{ }^{\circ}\text{C}$ ) and high  $\text{CO}_2/\text{CH}_4$  ratios. The side-reactions that contribute mostly to coke formation and deposition are:

Methane cracking:



Boudouard reaction:



The exothermic Boudouard reaction is disfavoured at higher temperatures ( $> 800\text{ }^{\circ}\text{C}$ ) and hence, beyond this temperature, the surface carbon formed is primarily produced by methane decomposition. Carbon formed by methane cracking is relatively more active and can be gasified by  $\text{CO}_2$ . Hence, operating at high reaction temperatures ( $> 800\text{ }^{\circ}\text{C}$ ) and high  $\text{CO}_2/\text{CH}_4$  ratios can be effective in inhibiting coke formation [1–4]. However, from an industrial point of view, it is desirable to operate at lower temperature and stoichiometric  $\text{CO}_2/\text{CH}_4$  ratio. Also, alternate methane sources like biogas have a  $\text{CO}_2/\text{CH}_4$  content of less than 1, making it even more challenging to prevent coke deposition [5].

Extensive research has been done over the last decade on designing coke-resistant Ni-based catalysts for dry reforming. Some of the approaches that have been shown to enhance coke-resistance are increasing metal-support interaction in the catalyst [6–8], doping basic metal oxides, introducing a second metal for bimetallic synergistic effect [9–12] etc. The formation of whisker carbon has been reported to increase with Ni particle size [13] and hence, sintering of Ni particles to form bigger particles at high temperature is considered a major cause of coke deposition. A recent development is the synthesis of novel metal@support core-shell structured catalysts which have shown significant resistance to metal sintering and coke formation [2]. Li et al. prepared a Ni@ $\text{SiO}_2$  catalyst from phyllosilicate precursors that showed excellent resistance to sintering and coke deposition in DRM at  $700\text{--}800\text{ }^{\circ}\text{C}$  [14]. Han et al. developed a  $\text{SiO}_2$  coated Ni nanoparticle@ $\text{SiO}_2$  sphere that showed stable performance for DRM at  $800\text{ }^{\circ}\text{C}$  for 170 h [15]. Similarly, Ni@ $\text{Al}_2\text{O}_3$  [16], Ni@ $\text{TiO}_2$  [17], Na@ $\text{ZrO}_2$  [18] core-shell catalysts have been developed, which show good stability in dry reforming. Confining nickel nanoparticles within the pores of ordered mesoporous supports have also shown promising results in minimizing coke formation in dry reforming [19–21]. However, most of these studies have been done at high reaction temperatures ( $> 700\text{ }^{\circ}\text{C}$ ) and a  $\text{CH}_4/\text{CO}_2$  ratio of 1 and the reported catalysts may not be as stable at lower operating temperatures or high  $\text{CH}_4/\text{CO}_2$  ratio as is expected in biogas. So far, there are few reports on Ni-based catalysts that can prevent coke formation in low temperature DRM ( $\leq 600\text{ }^{\circ}\text{C}$ ) [22].

In this study, we have synthesized an innovative sandwiched core-shell structured Ni- $\text{SiO}_2$ @ $\text{CeO}_2$  catalyst that showed high activity and stability at low temperature ( $600\text{ }^{\circ}\text{C}$ ) dry reforming of a model biogas mixture ( $\text{CH}_4/\text{CO}_2 = 3:2$ ) during a 72 h run with negligible coke formation. The unique sandwiched core-shell structure of the catalyst consists of a layer of nickel nanoparticles anchored between a spherical silica core and a thin cerium oxide shell. The dual confinement effect provided by the strong metal-support interaction between Ni and both the silica core and ceria shell prevents metal sintering and provides a physical barrier for the growth of carbon whiskers, which are known to uproot Ni from the support material. The cerium oxide shell, due to its redox property and high oxygen storage capacity, can gasify active carbon formed on the nickel metal by continuously supplying lattice oxygen. In fact, we observe that the cerium oxide shell causes a change in the mechanism of dry reforming from a mono-functional pathway on the Ni- $\text{SiO}_2$  catalyst to a bi-functional pathway on the ceria coated catalyst where the support sites are also involved in the reaction. The sandwiched core-shell Ni- $\text{SiO}_2$ @ $\text{CeO}_2$  catalyst showed far superior activity and coke inhibition than both Ni- $\text{SiO}_2$  (Ni-phyllosilicate-derived) and Ni- $\text{CeO}_2$  catalysts under same reaction conditions.

## 2. Experimental

### 2.1. Catalyst preparation

All chemicals were purchased from Sigma Aldrich and used without further pre-treatment. The reagents used were:  $\text{Ni}(\text{NO}_3)_2 \cdot 6\text{H}_2\text{O}$ ,  $\text{Ce}(\text{NO}_3)_3 \cdot 6\text{H}_2\text{O}$ , Tetra-ethyl orthosilicate (98%),  $\text{NH}_4\text{OH}$  solution (25%), Hexamethylenetetramine (99%), Ethanol Absolute (99.8%).

#### 2.1.1. Preparation of Ni- $\text{SiO}_2$ catalyst

Ni- $\text{SiO}_2$  catalysts were prepared via a Ni-phyllosilicate precursor route as reported before [23].  $\text{SiO}_2$  nano-spheres were first synthesized by a modified Stöber method [24]. 4 ml TEOS was added to 140 ml ethanol and a solution of 4.2 ml ammonia (25%) in 25 ml water was then added to the solution. The precipitation was allowed to continue for 24 h under stirring. Nickel phyllosilicate was formed on the synthesized  $\text{SiO}_2$  spheres by the ammonia evaporation method. Appropriate amount of Nickel nitrate hexahydrate was added to the synthesis solution mentioned above and the solution was heated at  $70\text{ }^{\circ}\text{C}$  until the pH reached 7. The mixture was then centrifuged, washed with ethanol and water and dried overnight in an oven. Nickel phyllosilicate supported on silica was finally obtained by calcining the solid obtained at  $700\text{ }^{\circ}\text{C}$  for 4 h. The catalyst was reduced in hydrogen *in-situ* at  $800\text{ }^{\circ}\text{C}$  before reaction and denoted as Ni- $\text{SiO}_2$ .

#### 2.1.2. Preparation of Ni- $\text{SiO}_2$ @ $\text{CeO}_2$ catalyst

250 mg of Nickel phyllosilicate supported on  $\text{SiO}_2$  and 330 mg Cerium nitrate hexahydrate was added to 40 ml ethanol. 5 g Hexamethylenetetramine dissolved in water was added to the previous mixture and heated to  $70\text{ }^{\circ}\text{C}$  for 7 h. The solid catalyst was recovered by centrifuging and subsequently washed with water and ethanol. The sample was calcined at  $700\text{ }^{\circ}\text{C}$  for 4 h and reduced in hydrogen *in-situ* at  $800\text{ }^{\circ}\text{C}$  before reaction. The catalyst is denoted as Ni- $\text{SiO}_2$ @ $\text{CeO}_2$ .

#### 2.1.3. Preparation of Ni- $\text{CeO}_2$ catalyst

A third catalyst, Ni- $\text{CeO}_2$  was synthesized by impregnation method and used as a reference to compare the dry reforming activity of the Ni- $\text{SiO}_2$ @ $\text{CeO}_2$  catalyst.  $\text{CeO}_2$  support was synthesized by calcining Cerium nitrate hexahydrate at  $400\text{ }^{\circ}\text{C}$  for 4 h. Appropriate amount of Nickel nitrate hexahydrate solution in water was added to the  $\text{CeO}_2$  support and stirred overnight at  $50\text{ }^{\circ}\text{C}$ . The Ni loading was kept at 10 wt%. The dried sample was then calcined in air at  $700\text{ }^{\circ}\text{C}$  for 4 h and reduced *in-situ* at  $800\text{ }^{\circ}\text{C}$  before reaction to produce Ni- $\text{CeO}_2$ .

### 2.2. Catalyst Characterization

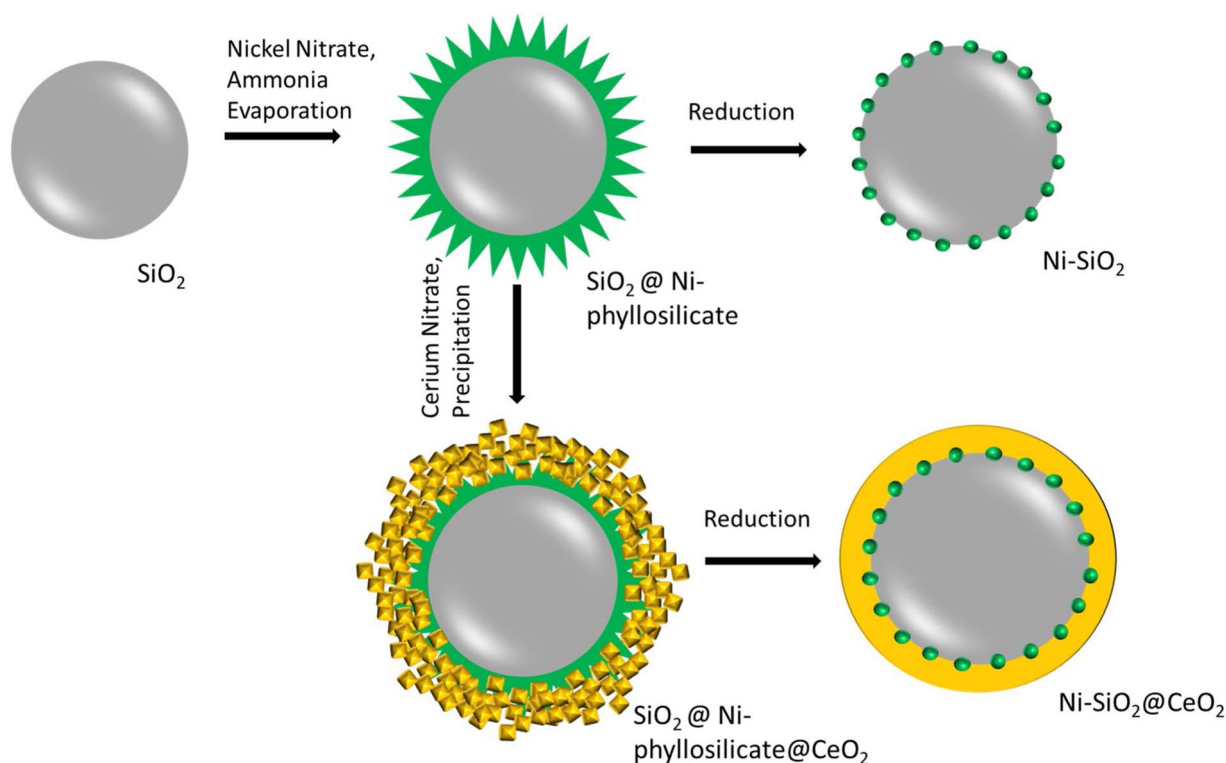
Morphology of the catalyst was examined by a JEOL JEM-2100 transmission electron microscope (TEM).

The X-ray diffraction (XRD) pattern of each sample was measured on a Shimadzu XRD-6000 diffractometer using  $\text{Cu K}\alpha$  radiation. All the catalysts were scanned at  $2\theta$  range between  $20^{\circ}$  to  $80^{\circ}$  (rate of  $2^{\circ}/\text{min}$ ).

The specific surface area of the fresh and spent catalysts was measured by nitrogen physical adsorption at  $77\text{ K}$  by an ASAP 2020 instrument, followed by calculated with the Brunauer–Emmett–Teller (BET) method.

Ni and Ce loading of the catalyst was measured with Thermal Scientific iCAP 6000 ICP-OES Analyser. 15 mg powder was dissolved in a mixture of 0.5 ml HF (48%), 2 ml  $\text{HNO}_3$  (65%), 2 ml  $\text{H}_2\text{O}_2$  (30%) and 40 ml DI water aided by ultrasonic treatment. Ni and Ce ICP standard solution diluted to appropriate concentrations was used to prepare the calibration curve.

X-ray photoelectron spectra (XPS) was performed in a Kratos AXIS Ultra DLD equipped with monochromatic Al  $\text{K}\alpha$  gun (photon energy of  $1486.6\text{ eV}$ ,  $225\text{ W}$ ) as the X-ray source and concentric hemispherical analyser. The results were referenced to the standard calibrated value of the adventitious carbon, C 1s hydrocarbon peak at  $284.6\text{ eV}$  prior to



**Scheme 1.** Schematic for synthesis of Ni-SiO<sub>2</sub> and Ni-SiO<sub>2</sub>@CeO<sub>2</sub> catalyst.

fitting the spectra of samples. All samples were reduced at 800 °C for 1 h under 30 ml/min hydrogen flow prior to testing.

H<sub>2</sub> Temperature-programmed reduction (TPR) measurements for the catalysts was performed on a Thermo Scientific TPDRO 1100 series system equipped with a thermal conductivity detector (TCD). Typically, 50 mg sample was tested with a flow of 5% hydrogen in nitrogen (30 ml/min) with a temperature ramping rate of 10 °C/min after degassing with helium for 10 min.

The metal dispersion measurement on catalyst was also done on a Thermo Scientific TPDRO 1100 series by a Hydrogen chemisorption method. 100 mg sample was first reduced by treating with a 5% hydrogen in nitrogen flow (30 ml/min) with a temperature ramp up to 800 °C and held for 1 h. The reduced sample was then cooled under nitrogen flow to an appropriate temperature (30 °C, 100 °C and 150 °C) and treated with 10 pulses of hydrogen of known volume. The moles of hydrogen chemisorbed was used to calculate the moles of surface nickel on the catalyst assuming that one hydrogen atom is adsorbed on one surface nickel atom. The average size of nickel crystallites was calculated from the equation  $d = (6 \times 10^3) / (g_{Ni} \times S_{Ni})$ , where  $g_{Ni}$  is the density of nickel and  $S_{Ni}$  is the surface area of nickel ( $m^2/g_{Ni}$ ), assuming that nickel crystallites are spherical, stoichiometry of hydrogen chemisorption is 1, and the surface area occupied by one atom of hydrogen equals to 0.065 nm<sup>2</sup> [25].

The carbon residue on the spent catalyst after dry reforming reaction was measured by thermo-gravimetric analysis (TGA) coupled with DTA (differential thermal analysis) on a Shimadzu DTG-60 thermo-gravimetric analyser. A fixed weight of spent catalyst was heated in static air to 850 °C with a ramping rate of 10 °C/min and its weight was monitored with temperature.

*In-situ* Diffuse Reflectance Infrared Fourier Transform Spectroscopy (DRIFTS) experiment was conducted in a Bruker FTIR Vertex 70 spectrometer using Harrick Praying Mantis DRIFTS gas cell equipped with ZnSe windows and a controlled gas system. Prior to testing, the catalyst was first reduced *ex-situ* at 800 °C for 1 h. The catalyst was then loaded into the DRIFTS cell and reduced again at 600 °C for 30 min under 15 ml/min H<sub>2</sub> flow. The remaining gas in the cell was flushed with

20 ml/min Helium flow for 1 h at 400 °C, following which a background scan was taken. The reaction mixture was then introduced into the cell (CH<sub>4</sub>/CO<sub>2</sub>/He = 2/2/20 ml/min) and the IR spectra were collected in the temperature range of 400 – 600 °C with a 50 °C step. The spectra were taken 32 times each with a resolution of 4 cm<sup>-1</sup>.

For DRIFTS study with pulsed flow of reactants, the catalyst was reduced *ex-situ* and then *in-situ* at 600 °C in the cell, followed by flushing with Helium for 2 h. The background scan was taken at 500 °C under He flow followed by introduction of a short pulse of methane. The IR spectra was collected every 20 s (repeated 4 times, resolution of 4 cm<sup>-1</sup>) after the pulse for 5 min. A CO<sub>2</sub> pulse of equal volume was then introduced followed by another methane pulse and IR spectra were collected with time.

The XAS experiments were carried out at XAFCA beamline of Singapore Synchrotron Light Source [26]. The samples were measured under transmission mode and Ni standard foil was applied for the energy calibration.

### 2.3. Catalytic evaluation

Biogas reforming was conducted in a quartz tube reactor with an inner diameter of 4 mm under atmospheric pressure. Before the reaction, the catalyst was reduced *in-situ* by pure H<sub>2</sub> (30 ml/min) at 800 °C for 1 h. The reaction temperature was set at 600 °C and undiluted model biogas with a composition of CH<sub>4</sub>/CO<sub>2</sub> of 3:2 was introduced at a GHSV of 200 L h<sup>-1</sup> g<sub>cat</sub><sup>-1</sup>. The flow rates of the gases were controlled by mass flow controllers and the composition of outlet gas was analysed online by a gas chromatograph (Agilent 7820A) equipped with a thermal conductivity detector (TCD). The GHSV was kept high so as to keep the conversion far below the equilibrium conversion and stay within the kinetic regime.

CO<sub>2</sub> and CH<sub>4</sub> conversion activity of the catalysts were calculated by following equations:

$$\text{Activity CO}_2 = \frac{\text{inlet CO}_2 - \text{outlet CO}_2 \text{ (mols/min)}}{\text{Ni content in catalyst (gram)}} \quad (4)$$

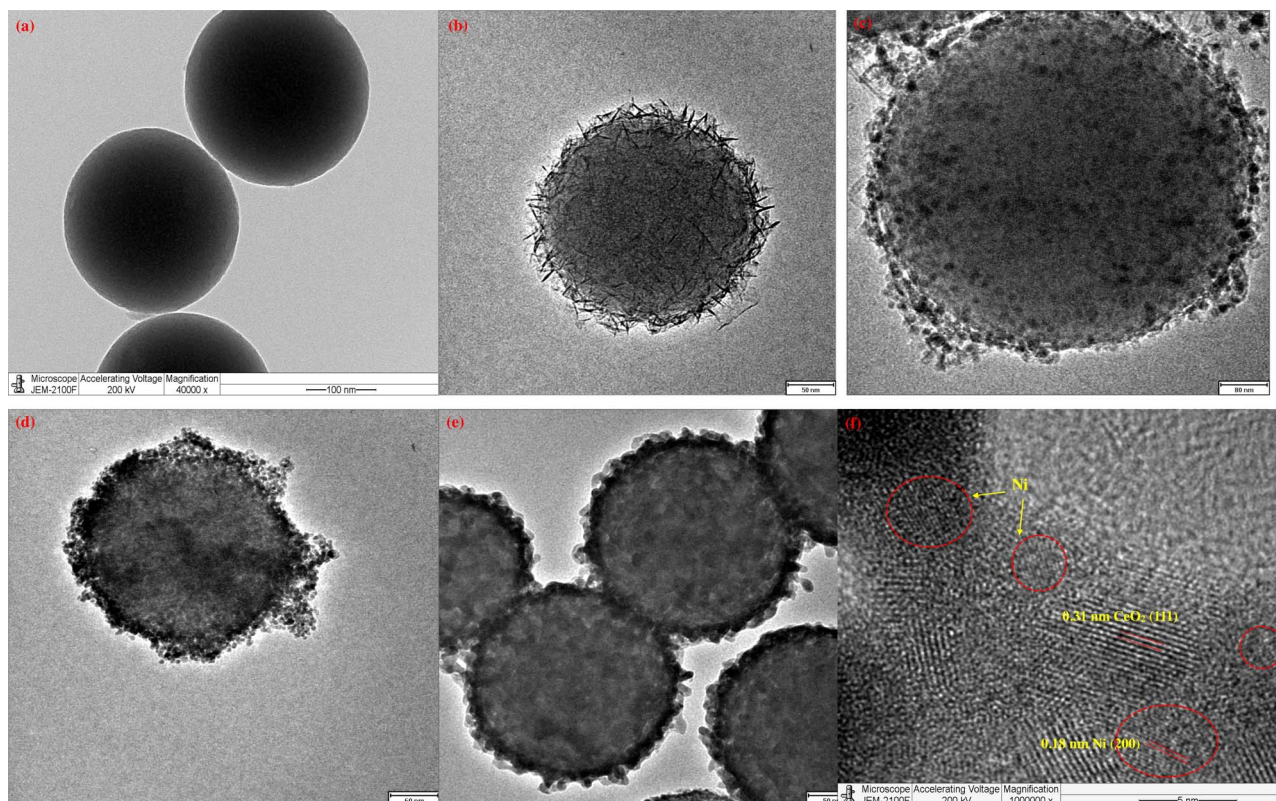


Fig. 1. TEM image for (a) SiO<sub>2</sub> nano-sphere (b) Ni-phyllsilicate supported on SiO<sub>2</sub> (c) reduced Ni-SiO<sub>2</sub> (d) CeO<sub>2</sub> coated Ni-phyllsilicate on SiO<sub>2</sub> (e) Reduced Ni-SiO<sub>2</sub>@CeO<sub>2</sub> (f) High resolution image of reduced Ni-SiO<sub>2</sub>@CeO<sub>2</sub> showing lattice fringes of CeO<sub>2</sub> and Ni.

$$\text{Activity CH}_4 = \frac{\text{inlet CH}_4 - \text{outlet CH}_4 \text{ (mols/min)}}{\text{Ni content in catalyst (gram)}} \quad (5)$$

The carbon balance and overall mass balance was  $\pm 5\%$  for all catalytic runs. Carbon balance was calculated as  $\frac{(\text{mols CH}_4 + \text{CO}_2 \text{ in inlet}) - (\text{mols CH}_4 + \text{CO}_2 + \text{CO in outlet})}{(\text{mols CH}_4 + \text{CO}_2 \text{ in inlet})} \times 100\%$ .

### 3. Results & discussion

#### 3.1. Characterization of fresh catalyst

##### 3.1.1. TEM analysis

The morphology of the freshly prepared and reduced catalysts was studied using TEM. Scheme 1 and Fig. 1(a–e) depict the schematic and TEM micrographs for the stepwise synthesis of the Ni-SiO<sub>2</sub> and Ni-SiO<sub>2</sub>@CeO<sub>2</sub> catalysts.

First, uniform silica nano-spheres of  $\sim 250$  nm diameter (Fig. 1a) were synthesized using the Stöber method [24]. This SiO<sub>2</sub> nano-sphere acts as an inert support and a silica source for the formation of a nickel phyllosilicate layer in the subsequent ammonia evaporation method. Nickel Phyllosilicate forms a thin layer of fibrous lamellae over the silica spheres (Fig. 1b) [2,28]. Upon reduction, this Ni-phyllsilicate layer decomposes to form Ni nanoparticles of size 5–10 nm dispersed uniformly on the spherical silica support (Fig. 1c).

For the preparation of Ni-SiO<sub>2</sub>@CeO<sub>2</sub>, the fresh Ni-phyllsilicate spheres were coated with a thin layer of CeO<sub>2</sub> using a precipitation method. CeO<sub>2</sub> precipitates in the form of small nanocrystals on the porous surface of the Ni-phyllsilicate spheres (Fig. 1d). Upon reduction, the ceria nanocrystals undergo a morphological change and a uniform layer of CeO<sub>2</sub> is formed which coats the Nickel nanoparticles supported on the silica spheres (Fig. 1e). The presence of Ni in the reduced Ni-SiO<sub>2</sub>@CeO<sub>2</sub> catalyst is confirmed using TEM-EDX mapping as the high density of the ceria over-layer makes it difficult to identify the Ni nanoparticles using just TEM. Fig. 2 shows the EDX mapping for a

reduced Ni-SiO<sub>2</sub>@CeO<sub>2</sub> catalyst. The relative intensities of the elements clearly reflect the sandwiched core-shell structure of the catalyst with an inert silica core and a thin ceria layer ( $\sim 10$  nm) with nickel nanoparticles uniformly dispersed on the silica core. Nickel nanoparticles embedded in ceria are also identified by their characteristic lattice fringes in a High Resolution TEM image, as shown in Fig. 1f [29–31].

TEM images of the fresh and reduced Ni-CeO<sub>2</sub> catalyst synthesized by impregnation method are shown in Fig. S1. In the reduced Ni-CeO<sub>2</sub> sample, Ni nanoparticles in the size range of 10–30 nm can be observed dispersed on a bulk CeO<sub>2</sub> support. Ni nanoparticles can be identified by its characteristic lattice fringes. Histogram in Fig. S2 exhibits the Ni particle size distribution observed by TEM for all catalysts.

##### 3.1.2. XRD analysis

Fig. 3 depicts the XRD patterns for the calcined and reduced catalysts. The calcined Ni-SiO<sub>2</sub> (pattern (a)) catalyst shows weak diffraction peaks at a  $2\theta$  value of 34, 37 & 61° characteristic of the nickel containing phyllosilicate phase [23,32]. A very weak peak is observed at 43.2° which shows that a small fraction of the Ni also exists in the NiO phase [27]. However, all peaks for the phyllosilicate phase are not clearly observed, which may be because of the weak crystallization of the phyllosilicate phase. In fact, it has been reported that the crystallinity of the phyllosilicate phase is highly affected by the preparation method, precipitation time and calcination temperature [33]. The broad XRD peak at 20–25° corresponds to the amorphous SiO<sub>2</sub> phase. Overall, the XRD pattern indicates a poorly crystallized Ni-phyllsilicate phase co-existing with a NiO and SiO<sub>2</sub> phase. The presence of Ni phyllosilicate phase is further confirmed with FT-IR analysis of the unreduced sample, which showed characteristic bands at 670, 710, 1024 and 3632 cm<sup>-1</sup> [34], [35]. The detailed analysis method and FT-IR spectrum (Fig. S3) is provided in the Supplementary Information.

The XRD pattern of the reduced Ni-SiO<sub>2</sub> (pattern (b)) catalyst shows diffraction peaks at 44.5 and 51.8° corresponding to metallic Ni phase

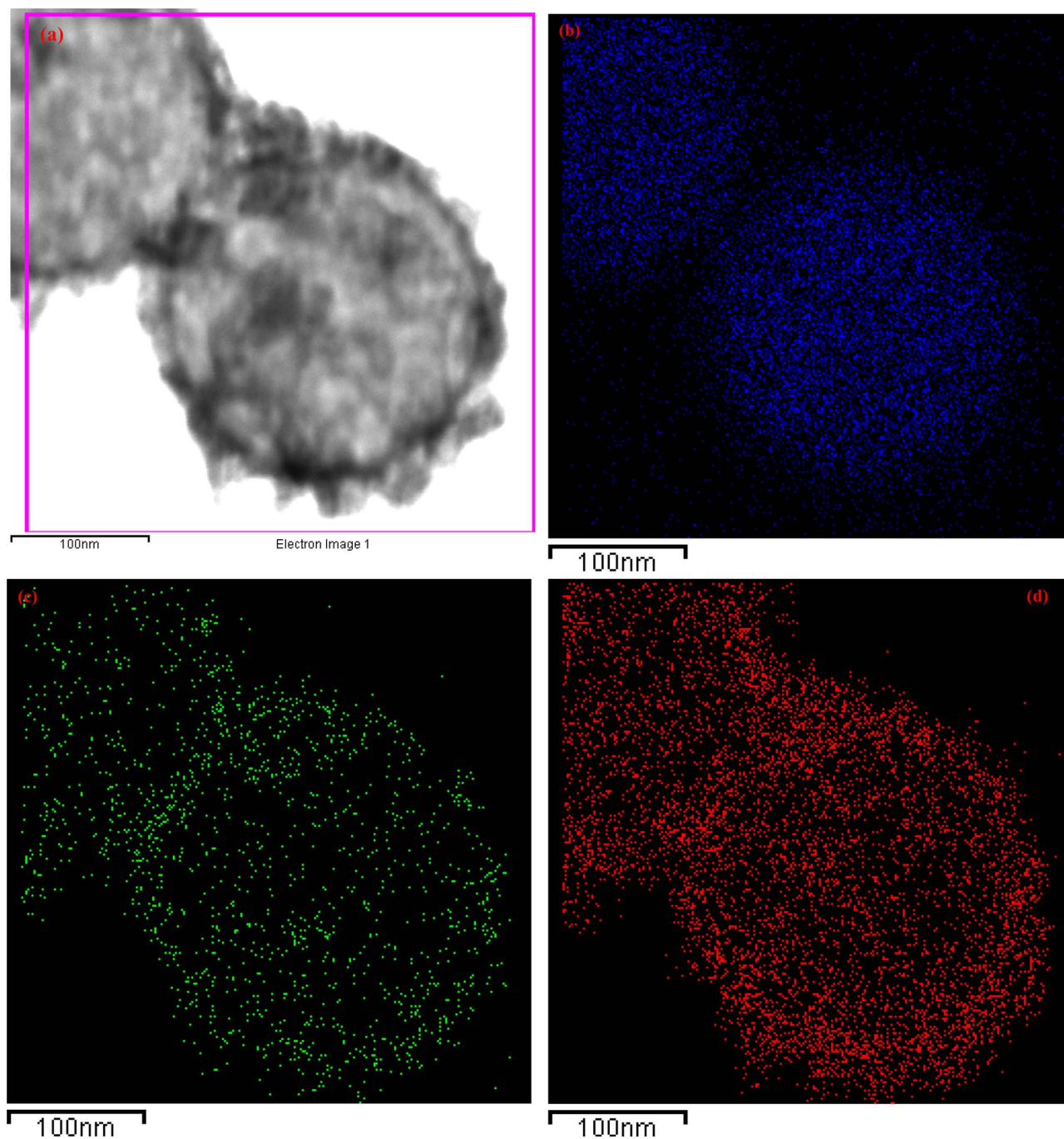


Fig. 2. TEM-EDX image of Reduced Ni-SiO<sub>2</sub>@CeO<sub>2</sub>. (a) TEM image of a Ni-SiO<sub>2</sub>@CeO<sub>2</sub> sphere, (b–d) Elemental mapping of Si, Ni and Ce respectively for image (a).

which show that the nickel phyllosilicate and NiO phases of the fresh catalyst have been reduced to form metallic nickel phase.

The XRD pattern for calcined Ni-SiO<sub>2</sub>@CeO<sub>2</sub> (pattern (c)) catalyst clearly shows the peaks for typical fluorite phase of CeO<sub>2</sub> at  $2\theta = 28.6, 33.1, 47.5, 56.4, 59.4, 69.6, 76.7$  and  $79.2^\circ$  in addition to the NiO and Ni-phyllosilicate phases. It is to be noted that a very weak and broad diffraction peak for metallic nickel phase is observed for the reduced Ni-SiO<sub>2</sub>@CeO<sub>2</sub> catalyst (pattern (d)), indicating that metallic Ni in Ni-SiO<sub>2</sub>@CeO<sub>2</sub> has lower crystallite size than Ni-SiO<sub>2</sub> catalyst [36]. This result is interesting because the same nickel phyllosilicate precursor is used to synthesize both Ni-SiO<sub>2</sub> and Ni-SiO<sub>2</sub>@CeO<sub>2</sub> catalyst; yet upon reduction, a distinct diffraction peak for metallic Ni is observed for Ni-SiO<sub>2</sub> while for the Ni-SiO<sub>2</sub>@CeO<sub>2</sub> catalyst, the Ni peak is broad and barely visible. This suggests that during the reduction of the catalyst,

the nickel species interacts with ceria, causing it to become more dispersed into smaller particles. HRTEM images of the reduced Ni-SiO<sub>2</sub>@CeO<sub>2</sub> catalyst (Fig. 1(f), S2) also show Ni particle sizes in the range of 3–5 nm, which is smaller than Ni particles on Ni-SiO<sub>2</sub> (6–8 nm), supporting the XRD results. This effect was also observed by Wang et al. in ceria doped Ni/Al<sub>2</sub>O<sub>3</sub> catalyst, where higher ceria doping reduced the Nickel particle size, making it impossible to detect Ni by XRD [37]. The reason was attributed to the redox character and higher dispersive character of CeO<sub>2</sub>, wherein the Ce<sup>4+</sup> / Ce<sup>3+</sup> redox couple creates surface and bulk oxygen vacancies that result in the formation of metal–oxygen complexes.

XRD pattern for Ni-CeO<sub>2</sub> prepared by impregnation method are consistent with previous reports [37] and are provided in Fig. S4. Diffraction peaks for NiO and CeO<sub>2</sub> and metallic Ni phases are observed for

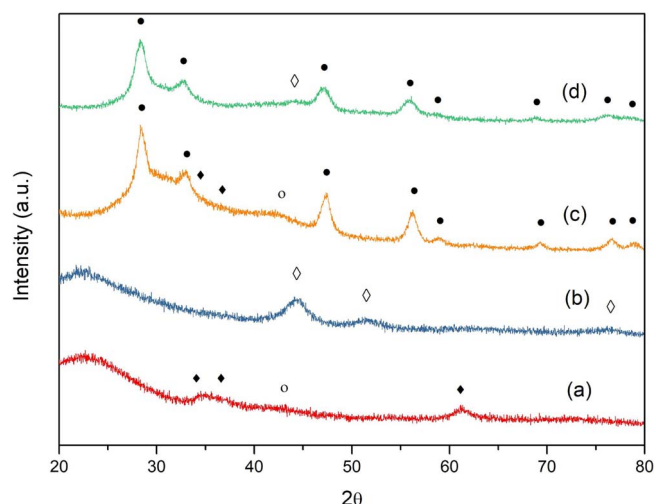


Fig. 3. XRD of (a) Fresh Ni-SiO<sub>2</sub> (b) Reduced Ni-SiO<sub>2</sub> (c) Fresh Ni-SiO<sub>2</sub>@CeO<sub>2</sub> (d) Reduced Ni-SiO<sub>2</sub>@CeO<sub>2</sub>. • CeO<sub>2</sub>, ○ NiO, ◇ Ni, ◆ Ni-phyllsilicate.

fresh and reduced Ni-CeO<sub>2</sub> catalyst respectively. Ni crystal size calculated from the Scherrer equation is 18.2 nm.

### 3.1.3. H<sub>2</sub>-TPR analysis

The reduction behaviour of the Ni-SiO<sub>2</sub> and Ni-SiO<sub>2</sub>@CeO<sub>2</sub> catalysts were investigated using H<sub>2</sub>-TPR and are presented in Fig. 4. The TPR profile for the Ni-SiO<sub>2</sub> catalyst can be divided into three main reduction peaks. The lower temperature reduction peak around 350–450 °C is attributed to the reduction of NiO to Ni<sup>0</sup> species with low interaction with the SiO<sub>2</sub> support while the reduction peak around 450–600 °C can be assigned to reduction of Ni<sup>2+</sup> in the 1:1 phyllosilicate structure with strong interaction with silica. The last peak around 690 °C can be associated with the reduction of 2:1 Nickel phyllosilicate, which is hardest to reduce [33,38].

The TPR profile for the Ni-SiO<sub>2</sub>@CeO<sub>2</sub> catalyst is distinctly different from the Ni-SiO<sub>2</sub> catalyst and includes contribution from the partial reduction of ceria as well. The low temperature reduction peak between 200–300 °C is assigned to the reduction of easily reducible oxygen species in oxygen vacancies formed by the replacement of Ce<sup>4+</sup> with Ni<sup>2+</sup> [39]. The entry of Ni<sup>2+</sup> ions into the ceria lattice causes lattice deformation and charge imbalance, forming oxygen vacancies, and the oxygen species adsorbed on the vacancies are easily reducible at low

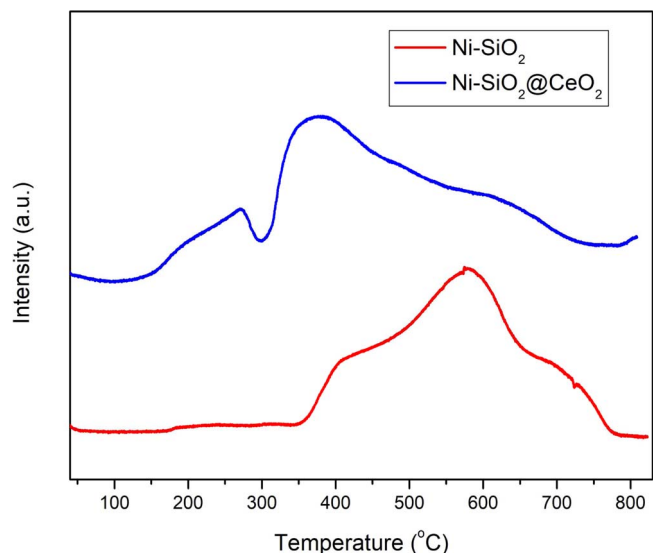


Fig. 4. H<sub>2</sub>-TPR profile for Ni-SiO<sub>2</sub> and Ni-SiO<sub>2</sub>@CeO<sub>2</sub>.

temperature. The broad peak starting at 300 °C is assigned to the reduction of NiO species and of surface Ce<sup>4+</sup> to Ce<sup>3+</sup> [39]. The high temperature reduction peak around 650 °C for Ni<sup>2+</sup> with strong interaction with SiO<sub>2</sub> is still observable but is much attenuated in intensity.

Table 1 shows the amount of H<sub>2</sub> consumed for nickel reduction up to 800 °C and percentage of Ni reduced in the Ni-SiO<sub>2</sub> and Ni-SiO<sub>2</sub>@CeO<sub>2</sub> catalysts. Since the TPR profile for Ni-SiO<sub>2</sub>@CeO<sub>2</sub> also includes the contribution from partial reduction of CeO<sub>2</sub>, TPR was conducted on SiO<sub>2</sub>@CeO<sub>2</sub> without any Ni content (Fig. S6) and the contribution for ceria reduction was subtracted from H<sub>2</sub> consumption of Ni-SiO<sub>2</sub>@CeO<sub>2</sub>. From Table 1, nickel is mostly reduced to metallic state in Ni-SiO<sub>2</sub>, but a small portion remains unreduced, likely in the phyllosilicate phase. On the other hand, the calculated extent of Ni reduction for Ni-SiO<sub>2</sub>@CeO<sub>2</sub> is slightly higher than 100% (~102.8%), which is because of the extra hydrogen consumed by the low temperature reduction of oxygen vacancies caused by entry of Ni<sup>2+</sup> in the CeO<sub>2</sub> lattice. Complete reduction of Ni in Ni-SiO<sub>2</sub>@CeO<sub>2</sub> is further evidenced by XANES analysis of the reduced catalyst in Section 3.3.4. Higher extent of Ni reduction and lower temperature of the reduction peak in Ni-SiO<sub>2</sub>@CeO<sub>2</sub> indicates that ceria promotes the reducibility of Nickel and allows reduction at lower temperatures. The promotion effect of CeO<sub>2</sub> on nickel reducibility is well accepted in literature and has been attributed to the ability of the doped CeO<sub>2</sub> to moderate the interaction of nickel with the support, thereby enhancing its reducibility [37,40,41].

The TPR profile for Ni-CeO<sub>2</sub> (Fig. S5) shows two reduction peaks – one around 200–350 °C for reduction of surface oxygen species formed by replacement of Ce<sup>4+</sup> by Ni<sup>2+</sup> in the ceria lattice and another around 350–500 °C for the reduction of NiO to Ni<sup>0</sup> and surface Ce<sup>4+</sup> to Ce<sup>3+</sup> species.

### 3.1.4. Textural and elemental analysis

The textural properties of the fresh and reduced catalysts were studied by N<sub>2</sub> isothermal adsorption-desorption (Table 1).

The fresh Ni-SiO<sub>2</sub> catalyst has a porous structure stemming from the porous lamellae of Ni-phyllsilicate. The average pore size is 12.1 nm which is consistent with previous reports [23]. The fresh Ni-SiO<sub>2</sub>@CeO<sub>2</sub> catalyst has lower surface area and pore volume than the Ni-SiO<sub>2</sub> catalyst because the ceria nanoparticles deposit on the porous branches of the phyllosilicate structure and blocks some pores. Upon reduction, the surface area of both catalysts was decreased, which is primarily because of the collapse of the porous phyllosilicate structure. It is interesting to note that the average pore size for the reduced Ni-SiO<sub>2</sub>@CeO<sub>2</sub> catalyst is in the mesoporous region, which suggests that the thin CeO<sub>2</sub> shell (~10 nm) may not provide significant diffusional resistance to the small reactant/product molecules during reforming reaction.

The Ni loading for the fresh Ni-SiO<sub>2</sub> catalyst was measured to be 8.63% by ICP-OES. Since the same Ni-SiO<sub>2</sub> core is used to synthesize the Ni-SiO<sub>2</sub>@CeO<sub>2</sub> catalyst, the Ni loading for the latter is lower (5.29%) due to the addition of CeO<sub>2</sub>.

### 3.1.5. XPS analysis

XPS was carried out to understand the surface nickel species in the freshly reduced catalysts. Fig. 5a shows the 2p binding energies (BE) for the reduced Ni-SiO<sub>2</sub> and Ni-SiO<sub>2</sub>@CeO<sub>2</sub> catalysts. For the reduced Ni-SiO<sub>2</sub> catalyst, peaks for Ni<sup>0</sup> 2p<sub>3/2</sub> and Ni<sup>0</sup> 2p<sub>1/2</sub> BE's are observed at 852.7 and 870 eV respectively [42]. Apart from metallic Ni peaks, a small peak is also observed at 856.4 eV that is assigned to Ni<sup>2+</sup> in a 2:1 phyllosilicate phase [43]. This indicates that even after reduction at 800 °C, some of the Ni species remains in the phyllosilicate phase, which is in agreement with TPR results.

The spectra for reduced Ni-SiO<sub>2</sub>@CeO<sub>2</sub> do not show any distinct peak for nickel species, which indicates that the surface concentration of nickel species in reduced Ni-SiO<sub>2</sub>@CeO<sub>2</sub> is almost negligible. It is known that the detectable depth of XPS spectroscopy is around 5 nm, and in our case, the thickness of the ceria shell over the Ni is ~10 nm,

**Table 1**  
Textural Properties and Metal Content of catalysts.

Catalyst	Surface area <sup>a</sup> (m <sup>2</sup> g <sup>−1</sup> )	Pore Volume <sup>a</sup> (cm <sup>3</sup> g <sup>−1</sup> )	Pore Size <sup>a</sup> (nm)	Ni loading <sup>b</sup> (wt %)	Ce loading <sup>b</sup> wt %	H <sub>2</sub> consumed in TPR for Ni reduction (mmol/ g <sub>cat</sub> )	Ni reduction extent (%)
Ni-SiO <sub>2</sub> (fresh)	95.94	0.293	12.1	8.63	nil	1.395	94.9
Ni-SiO <sub>2</sub> (reduced)	61.78	0.140	9.1				
Ni-SiO <sub>2</sub> @CeO <sub>2</sub> (fresh)	49.91	0.144	11.7	5.29	27.7	0.927 <sup>c</sup>	102.8
Ni-SiO <sub>2</sub> @CeO <sub>2</sub> (reduced)	31.95	0.123	15.7				

<sup>a</sup> Measured by N<sub>2</sub> isotherm adsorption-desorption, surface area and pore size were calculated with BET method and pore volume was calculated with BJH method.

<sup>b</sup> Measured by ICP-OES.

<sup>c</sup> H<sub>2</sub> consumption only for Ni reduction calculated after subtracting H<sub>2</sub> consumption from CeO<sub>2</sub> reduction (0.867 mmol H<sub>2</sub>/g<sub>cat</sub>).

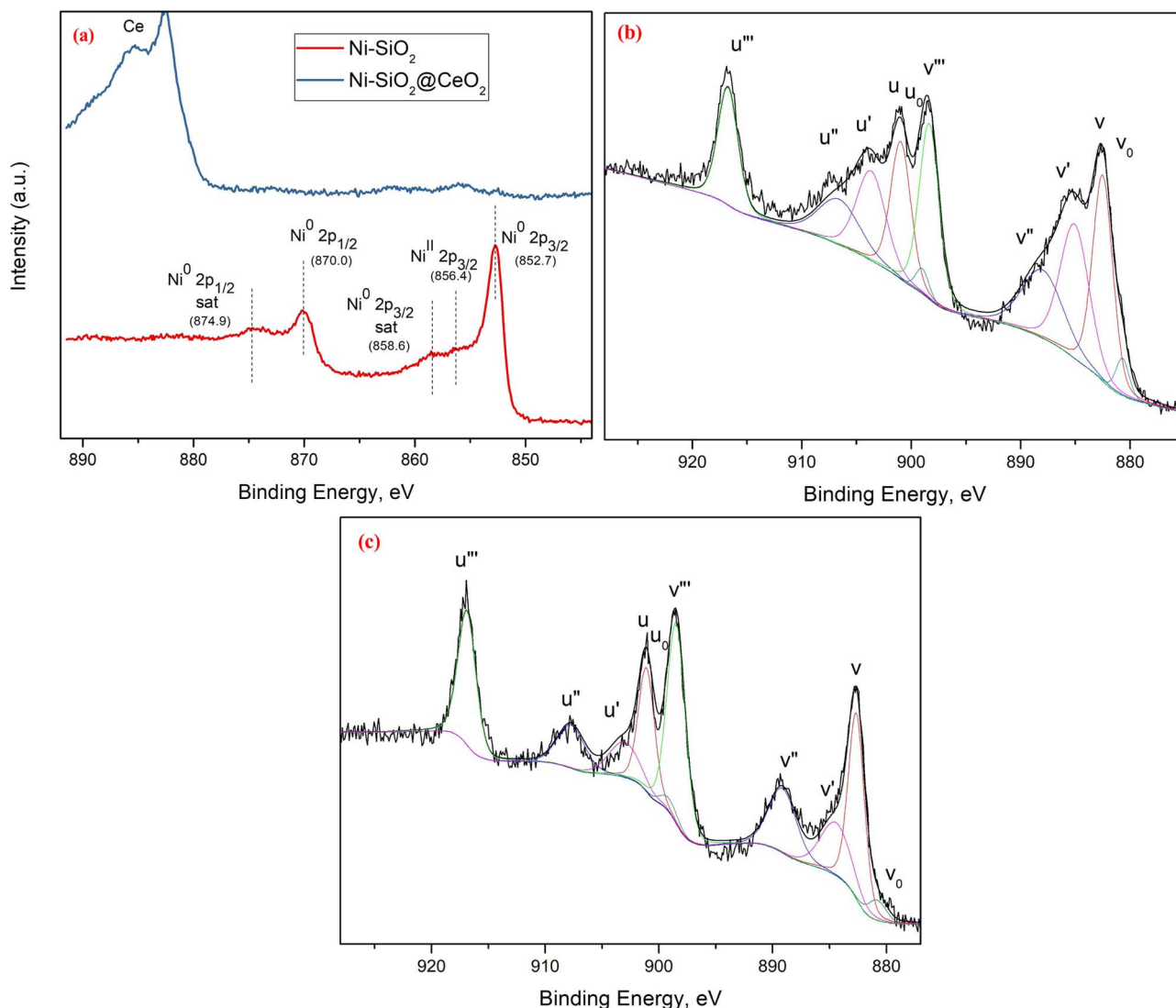
because of which the nickel species cannot be detected by XPS. Thus, this result further supports the core-shell structure of the catalyst, where all the nickel particles are covered with a CeO<sub>2</sub> shell.

Fig. 5b and c shows the Ce 3d spectra for reduced Ni-SiO<sub>2</sub>@CeO<sub>2</sub> and Ni-CeO<sub>2</sub> respectively. The spectra were deconvoluted into ten peaks due to Ce 3d<sub>5/2</sub> (labelled as v) and Ce 3d<sub>3/2</sub> (labelled as u) contributions. The v, v', v'' bands are attributed to Ce<sup>4+</sup> and v° and v' bands are attributed to Ce<sup>3+</sup>. It has been widely reported that the existence of Ce<sup>3+</sup> in ceria is associated with the formation of oxygen vacancies, and higher concentration of Ce<sup>3+</sup> implies larger amounts of oxygen vacancies [44]. The relative Ce<sup>3+</sup> concentration on the catalyst surface is

calculated as  $\text{Ce}^{3+}/(\text{Ce}^{3+} + \text{Ce}^{4+})$ . The Ni-SiO<sub>2</sub>@CeO<sub>2</sub> catalyst shows a much higher concentration of Ce<sup>3+</sup> { $\text{Ce}^{3+}/(\text{Ce}^{3+} + \text{Ce}^{4+}) = 0.295$ } compared to Ni-CeO<sub>2</sub> { $\text{Ce}^{3+}/(\text{Ce}^{3+} + \text{Ce}^{4+}) = 0.191$ }. This shows that the reduced Ni-SiO<sub>2</sub>@CeO<sub>2</sub> catalyst has higher amount of oxygen vacancies compared to reduced Ni-CeO<sub>2</sub> catalyst, which can be explained by the lower crystallite size and higher dispersion of ceria in Ni-SiO<sub>2</sub>@CeO<sub>2</sub> [45].

### 3.1.6. H<sub>2</sub> pulse chemisorption

H<sub>2</sub> pulse chemisorption was done to determine the accessible nickel sites on the reduced catalysts. H<sub>2</sub> chemisorption was conducted at three



**Fig. 5.** XPS Profile for (a) Ni 2p for Ni-SiO<sub>2</sub> and Ni-SiO<sub>2</sub>@CeO<sub>2</sub>, (b) Ce 3d for Ni-SiO<sub>2</sub>@CeO<sub>2</sub>, (c) Ce 3d for Ni-CeO<sub>2</sub>.

**Table 2**  
Ni Dispersion measurement by H<sub>2</sub> chemisorption.

Catalyst	H <sub>2</sub> chemisorbed (μmol H <sub>2</sub> g <sub>cat</sub> <sup>−1</sup> )			Ni loading (wt%)	Ni Dispersion <sup>a</sup> (wt%)	Estimated Ni particle size <sup>a</sup> (nm)
	30 °C	100 °C	150 °C			
Ni-SiO <sub>2</sub>	47.4	67.2	58.7	8.63	9.15	11.04
Ni-SiO <sub>2</sub> @CeO <sub>2</sub>	0.7	2.9	1.7	5.29	0.63	158.8

<sup>a</sup> Calculated based on H<sub>2</sub> chemisorption at 100 °C.

different temperatures, 30 °C, 100 °C and 150 °C. The amount of hydrogen chemisorbed was highest at 100 °C and subsequently decreased at higher temperature [25]. From the amount of chemisorbed hydrogen at 100 °C, the Ni metal dispersion in reduced Ni-SiO<sub>2</sub> catalyst was calculated to be 9.15% (Table 2). The Ni crystal size calculated from chemisorption results on Ni-SiO<sub>2</sub> is ~11 nm, which is slightly higher than the observations from TEM (6–8 nm). The higher nickel crystallite size estimation from H<sub>2</sub> chemisorption may be because the Ni-phyll-silicate derived Ni particles are partially embedded in the support [46], causing some of the nickel surface to be unavailable for chemisorption.

On the other hand, the hydrogen chemisorption on Ni-SiO<sub>2</sub>@CeO<sub>2</sub> catalyst was very low at all tested temperatures (Table 2), indicating that surface Ni sites are not available for hydrogen chemisorption. Even at 100 °C which corresponds to the maximum amount of chemisorption, the estimated nickel crystallite size for Ni-SiO<sub>2</sub>@CeO<sub>2</sub> from chemisorption results is > 150 nm, which is clearly very different from TEM or XRD observations. This inability to chemisorb hydrogen is likely caused by the coverage of nickel surface by ceria in the core-shell catalyst and/or by the strong metal support interaction (SMSI) between ceria and nickel, which blocks the Ni active sites for hydrogen chemisorption. The inability to chemisorb hydrogen by Ni-CeO<sub>2</sub> catalysts has also been previously observed by Uner et al. for Ni-CeO<sub>2</sub> catalysts due to SMSI effect [47]. It is important to note that this strong interaction between nickel and ceria is beneficial for coke resistance in dry reforming reactions because it imparts higher stability to the nickel particles. The inability of Ni-SiO<sub>2</sub>@CeO<sub>2</sub> catalyst to chemisorb hydrogen at room temperature does not, however, mean that active nickel sites are not available for methane reforming at DRM conditions, as is apparent from the catalyst performance (Figs. 6 and 7) and reported literature [47,48].

As we are not able to accurately quantify the number of active sites for the Ni-SiO<sub>2</sub>@CeO<sub>2</sub> catalyst from the H<sub>2</sub> chemisorption technique, we report the specific activity of the catalyst in terms of moles of reactant converted per gram of nickel per unit time [14,49].

## 3.2. Catalyst performance and stability for dry reforming of bio-gas

### 3.2.1. Bio-gas reforming activity

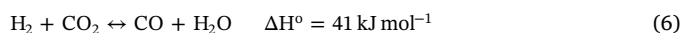
The catalytic performance of Ni-SiO<sub>2</sub>, Ni-SiO<sub>2</sub>@CeO<sub>2</sub> and Ni-CeO<sub>2</sub> catalysts was tested for dry reforming of bio-gas with a CH<sub>4</sub>/CO<sub>2</sub> ratio of 3:2 for the temperature range of 600 °C to 750 °C. Reaction was carried out at high GHSV (200L/h g catalyst) to ensure that the conversion was much lower than equilibrium conversion to reflect the true activity of catalyst.

Fig. 6(a)–(c) shows the CH<sub>4</sub> and CO<sub>2</sub> conversion rate and H<sub>2</sub>/CO ratio for Ni-SiO<sub>2</sub>, Ni-SiO<sub>2</sub>@CeO<sub>2</sub> and Ni-CeO<sub>2</sub> catalysts respectively. Ni-CeO<sub>2</sub> catalyst showed the lowest activity. The poor activity may be explained by the low Ni dispersion (see Figs. S1 and S2) and poor thermal stability of CeO<sub>2</sub> as a support. Additionally, the SMSI effect for Ni-CeO<sub>2</sub>, especially after reduction at high temperature, can also contribute to attenuated activity of the catalyst. Uner et al. reported that a thin coating of CeO<sub>2</sub> on Ni was formed in Ni-CeO<sub>2</sub> catalysts that led to very strong metal support interaction between Ni and CeO<sub>2</sub> [47]. This SMSI imparted high coke-resistance to the catalyst but at the same time,

suppressed the catalyst activity.

Out of the other two catalysts, Ni-SiO<sub>2</sub>@CeO<sub>2</sub> shows much higher activity than the Ni-SiO<sub>2</sub> catalyst at all temperatures. This higher activity can be attributed to the higher Ni dispersion and the higher reducibility of the Ni-SiO<sub>2</sub>@CeO<sub>2</sub> catalyst than Ni-SiO<sub>2</sub>, as can be observed from TEM, XRD and TPR results. We expect that the encapsulation of Ni by CeO<sub>2</sub> in the Ni-SiO<sub>2</sub>@CeO<sub>2</sub> catalyst and the consequent SMSI does have a suppressing effect on the activity of Ni, but it is outweighed by the increase in activity due to the higher Ni dispersion. Also, compared to Ni-CeO<sub>2</sub>, we believe that the metal support interaction in between Ni and CeO<sub>2</sub> is lower in Ni-SiO<sub>2</sub>@CeO<sub>2</sub> because there is a strong interaction between Ni and SiO<sub>2</sub>, which may moderate the interactions between Ni and CeO<sub>2</sub>.

For all the catalysts, the CO<sub>2</sub> conversion is higher than the CH<sub>4</sub> conversion, which is because of the reverse water gas shift reaction occurring simultaneously with dry reforming of methane. As a result, the H<sub>2</sub>/CO ratio is always lower than 1.



The H<sub>2</sub>/CO ratio achieved over the Ni-SiO<sub>2</sub>@CeO<sub>2</sub> and Ni-CeO<sub>2</sub> catalysts is slightly lower than that for Ni-SiO<sub>2</sub> catalyst. This is because of the higher CO<sub>2</sub> conversion on ceria due to adsorption and activation of CO<sub>2</sub> on the oxygen vacancies in the ceria support and on the Ni/ceria interface [50,51]. Ni/ceria is known to be an efficient water gas shift (WGS) catalyst. Thus, at high temperatures, the reverse water gas shift (RWGS) is highly favoured on the Ni-SiO<sub>2</sub>@CeO<sub>2</sub> and Ni-CeO<sub>2</sub> catalyst leading to lower H<sub>2</sub>/CO ratio.

### 3.2.2. Catalyst stability

Fig. 7 shows the stability test of Ni-SiO<sub>2</sub>, Ni-SiO<sub>2</sub>@CeO<sub>2</sub> and Ni-CeO<sub>2</sub> for dry reforming of biogas at 600 °C. We have conducted the stability test at 600 °C because inactive coke accumulation is most severe at low temperature for dry reforming [3,52].

The Ni-SiO<sub>2</sub> catalyst shows an initial methane conversion of 0.09 mol min<sup>−1</sup> gNi<sup>−1</sup> and a CO<sub>2</sub> conversion of 0.13 mol min<sup>−1</sup> gNi<sup>−1</sup>. The H<sub>2</sub>/CO ratio is lower than 1 due to the concurrent occurrence of RWGS reaction, which is quite prominent at the reaction temperature of 600 °C. After an initial drop, the activity of the Ni-SiO<sub>2</sub> catalyst remained quite stable but the catalyst showed a high coke accumulation rate that blocked the catalyst bed within 22 h and increased the back-pressure in the reactor, preventing the reactant gases from entering the reactor.

The Ni-SiO<sub>2</sub>@CeO<sub>2</sub> catalyst, on the other hand, maintains a stable performance throughout the 72-hour run undergoing only 10% loss in activity over the entire duration. In contrast to the Ni-SiO<sub>2</sub> catalyst, there is no build-up of pressure in the reactor over the 72 h TOS, indicating no bed blocking by coke deposition.

The Ni-CeO<sub>2</sub> catalyst also shows a stable performance over 72 h at a much lower conversion. Fig. S7(a–c) shows the amounts of reactants converted and products measured for this catalytic run for the different catalysts.

## 3.3. Spent catalyst characterization

The spent catalysts were characterized by TGA, XRD, TEM and XANES.

### 3.3.1. TGA analysis

Coke accumulation on the Ni-SiO<sub>2</sub> catalyst was confirmed by TGA coupled with DTA of the spent catalyst (Fig. 8). TGA of the spent Ni-SiO<sub>2</sub> catalyst shows a dramatic weight loss in the region of 480–660 °C, and the DTA exhibits a corresponding exothermic peak indicating the combustion of deposited coke. The high temperature of coke oxidation show that the coke deposited is mostly filamentous or graphitic in nature [53].

On the other hand, the TGA of the spent Ni-SiO<sub>2</sub>@CeO<sub>2</sub> catalyst after 72 h reaction shows negligible weight loss and no detectable

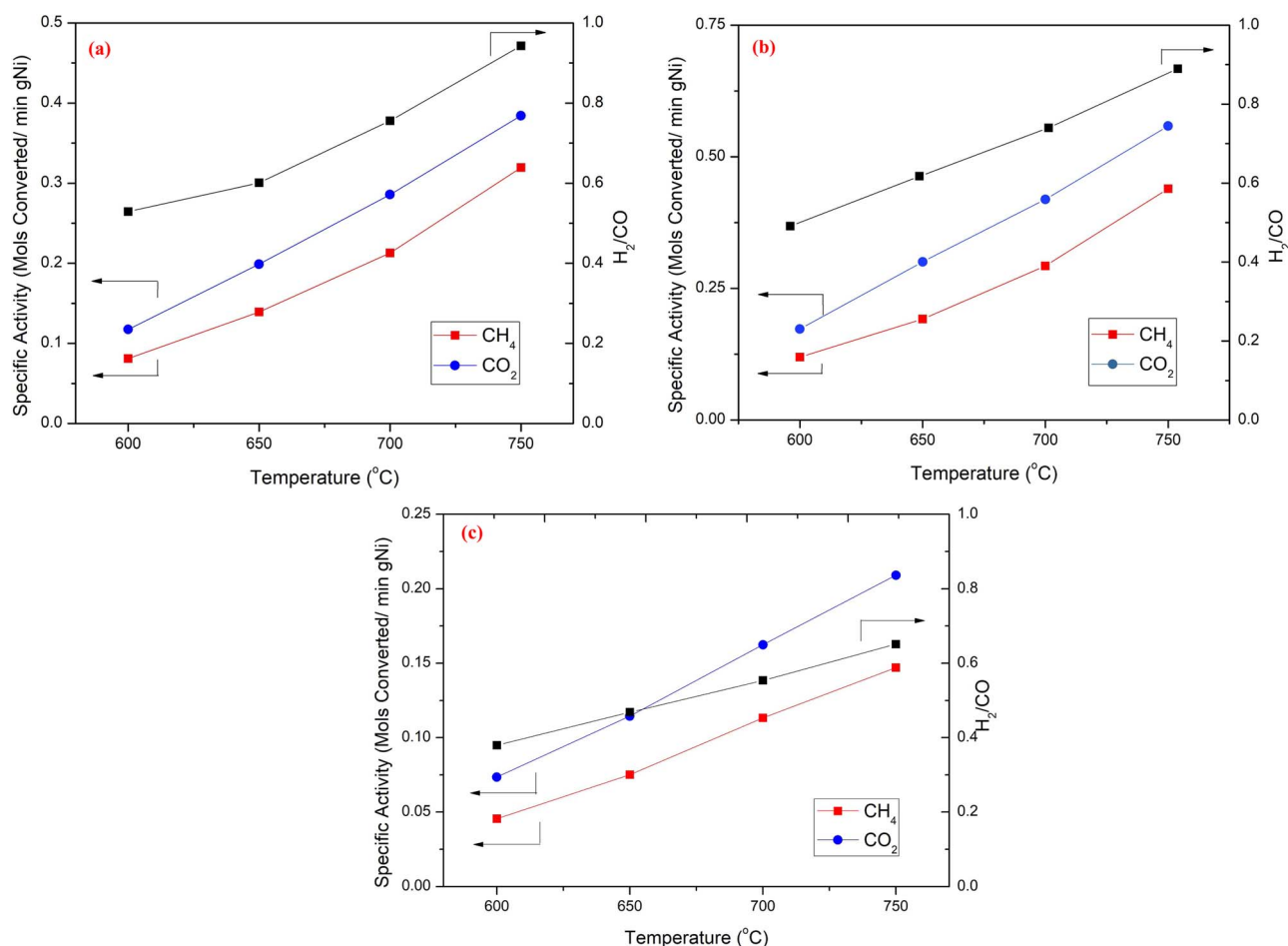


Fig. 6. Specific Activity of (a) Ni-SiO<sub>2</sub>, (b) Ni-SiO<sub>2</sub>@CeO<sub>2</sub> and (c) Ni-CeO<sub>2</sub> for bio-gas reforming at 600 °C–750 °C. Reaction Conditions: GHSV = 200 L h<sup>-1</sup> g<sub>cat</sub><sup>-1</sup>, CH<sub>4</sub>: CO<sub>2</sub> = 3:2.

exotherm in the temperature range of 480–700 °C, indicating that coke accumulation on the spent catalyst is negligible. The initial weight gain observed in the TGA profile is because of the re-oxidation of Ni and partially reduced CeO<sub>2</sub> in the spent catalyst.

Interestingly, the spent Ni-CeO<sub>2</sub> catalyst after 72 h of reaction shows ~4.5% weight loss in TGA. High stability and low coke formation on Ni-CeO<sub>2</sub> is expected because of the redox nature of the CeO<sub>2</sub> support, but compared to Ni-SiO<sub>2</sub>@CeO<sub>2</sub> which has much less ceria content, the Ni-CeO<sub>2</sub> catalyst clearly shows higher coke deposition. It is likely that the large Ni particle size in Ni-CeO<sub>2</sub> accelerates the formation of coke, which cannot be completely oxidized by the ceria lattice oxygen.

### 3.3.2. XRD analysis

The XRD of the spent Ni-SiO<sub>2</sub> catalyst (Fig. 9) shows peaks at  $2\theta = 26.5$  and  $42.4^\circ$  for graphitic phase in the multiwalled carbon nanotubes that are formed during the reaction [54]. Peaks for metallic Ni<sup>0</sup> are also observed at  $2\theta = 44.5^\circ$  and  $51.8^\circ$ .

In line with TGA results, the XRD profile for the spent Ni-SiO<sub>2</sub>@CeO<sub>2</sub> catalyst shows no peak for carbon. Also, there is no detectable peak for Ni<sup>0</sup> in the spent Ni-SiO<sub>2</sub>@CeO<sub>2</sub> catalyst, suggesting that sintering of nickel particles during reaction is minimal. XRD peaks observed for CeO<sub>2</sub> at  $2\theta = 28.6, 33.1, 47.5, 56.4$  &  $76.7^\circ$  in the spent catalyst are broader and weaker than those for the reduced catalyst.

For Ni-CeO<sub>2</sub>, a small peak for graphitic carbon is observable in the XRD spectrum of the spent catalyst (Fig. S4).

### 3.3.3. TEM analysis

TEM micrographs of the spent Ni-SiO<sub>2</sub> catalyst (Fig. 10a–b) show extensive growth of carbon whiskers. Fig. 10b shows a magnified image

of a carbon nanotube on the spent Ni-SiO<sub>2</sub> catalyst with a nickel particle at the tip, showing that the filamentous carbon has captured the nickel particle and uprooted it from the silica support. The formation of filamentous carbon does not deactivate the nickel surface but causes a breakdown of the catalyst by pore-plugging [77]. The uncontrolled growth of carbon whiskers thus causes an expansion of the reactor bed and leads to complete bed blocking in severe cases as we observe here. Sintering of Ni particles is also observed in the spent Ni-SiO<sub>2</sub> TEM images. Fig. S8a shows a Ni particle size distribution for the spent Ni-SiO<sub>2</sub> catalyst, which shows that the majority of Ni particles are higher than 10 nm in the spent catalyst.

On the contrary, TEM images of the spent Ni-SiO<sub>2</sub>@CeO<sub>2</sub> catalyst (Fig. 10c) do not show the growth of filamentous carbon. From the Ni particle size distribution in the spent catalyst (Fig. S8b), we can see that there is very less sintering with the average Ni particle size increasing from 3–5 nm to 4–6 nm only over 72 h and no Ni particles observed above 10 nm.

Formation of whisker carbon is observed on Ni-CeO<sub>2</sub> (Fig. 10d), in line with TGA and XRD results. Substantial sintering of Ni is also observed on the spent Ni-SiO<sub>2</sub> catalyst (Fig. S8c).

Thus, we see that the CeO<sub>2</sub> shell reduces metal sintering and effectively eliminates the formation and deposition of coke even at conditions that favour coke formation (low temperature and high CH<sub>4</sub>/CO<sub>2</sub> ratio), making the catalyst an excellent candidate for low temperature bio-gas reforming reaction. The Ni-SiO<sub>2</sub>@CeO<sub>2</sub> catalyst is superior to both the Ni-SiO<sub>2</sub> and Ni-CeO<sub>2</sub> catalyst in terms of activity and coke resistance. Table 3 shows a comparison of the coke inhibition property of the Ni-SiO<sub>2</sub>@CeO<sub>2</sub> catalyst with some of the recent Ni-based catalysts developed for carbon free dry reforming reaction [5,20,23,55–67]. It is

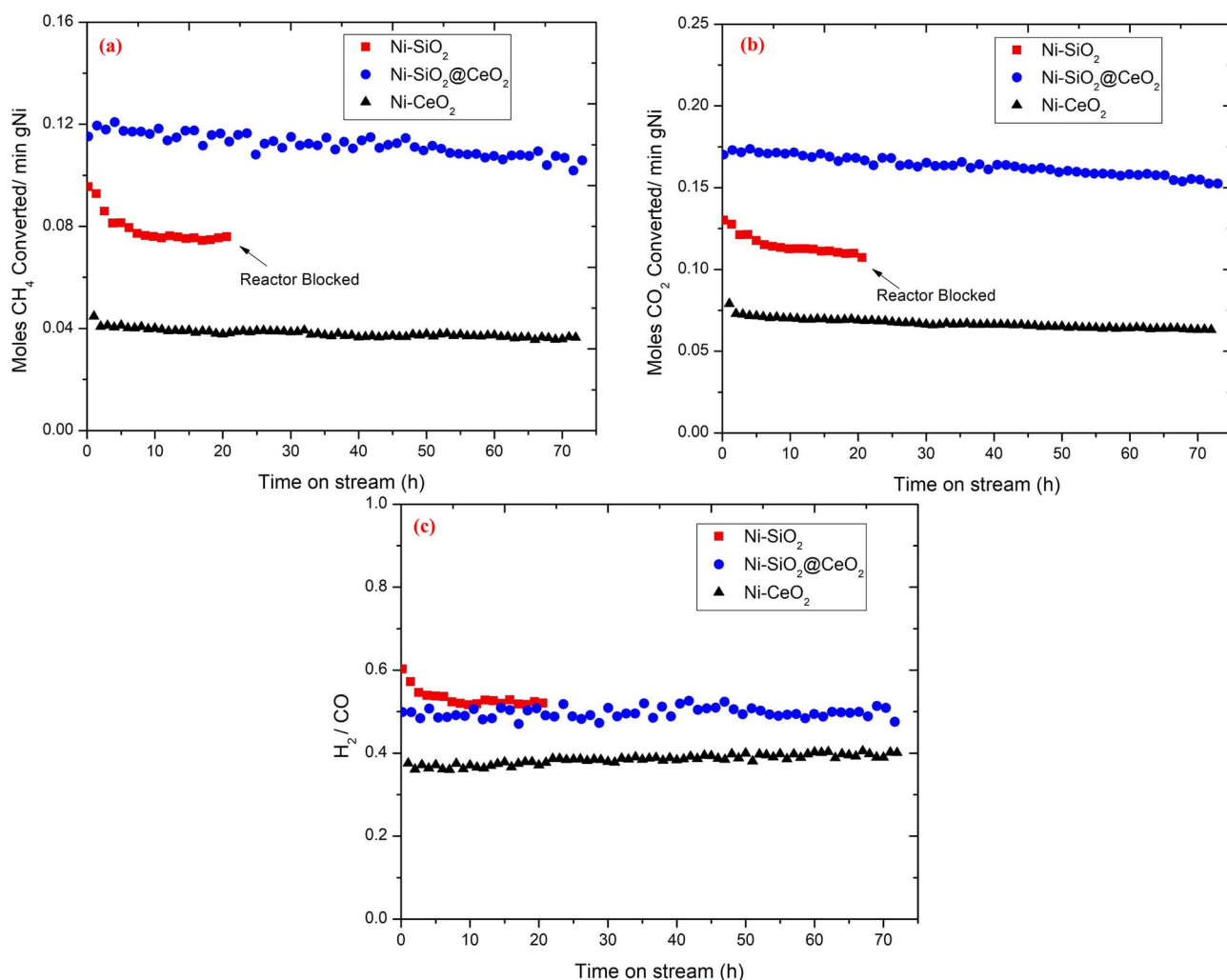


Fig. 7. Long term stability test for dry reforming of bio-gas at 600 °C; (a) Specific activity for CH<sub>4</sub> conversion, (b) Specific Activity for CO<sub>2</sub> conversion, (c) H<sub>2</sub>/CO ratio. Reaction Conditions: GHSV = 200 L h<sup>-1</sup> g<sub>cat</sub><sup>-1</sup>, CH<sub>4</sub>:CO<sub>2</sub> = 3:2.

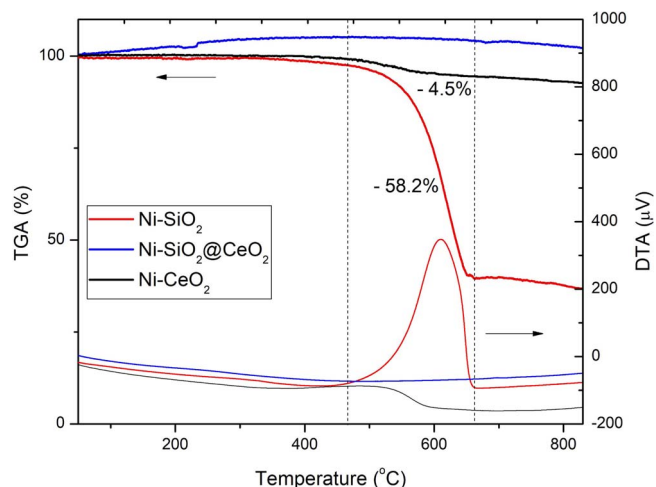


Fig. 8. TGA and DTA analysis of spent catalyst - Ni-SiO<sub>2</sub> after 22 h, Ni-SiO<sub>2</sub>@CeO<sub>2</sub> after 72 h, Ni-CeO<sub>2</sub> catalyst after 72 h of bio-gas reforming at 600 °C.

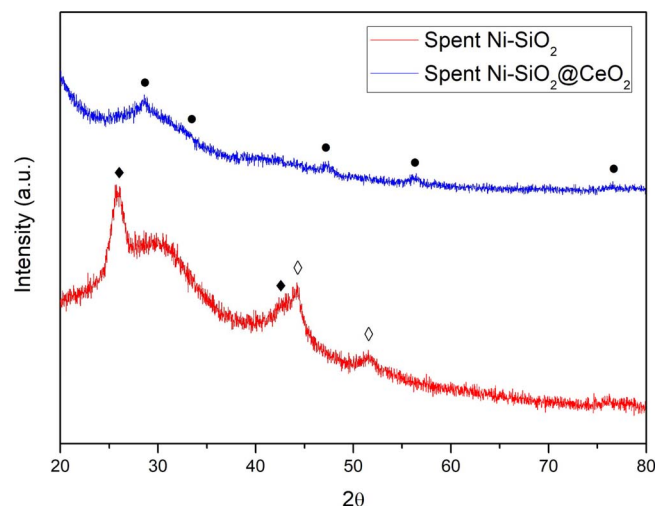


Fig. 9. XRD pattern for spent catalyst - Ni-SiO<sub>2</sub> after 22 h and Ni-SiO<sub>2</sub>@CeO<sub>2</sub> after 72 h of bio-gas reforming at 600 °C. ◇ Ni, ◆ Graphite, • CeO<sub>2</sub>.

to be noted that most of the stability tests cited in Table 3 were conducted at high temperatures and low CH<sub>4</sub>/CO<sub>2</sub> ratio or with dilution by inert gas, which favour lower carbon deposition when compared to the conditions used in this study. While this is by no means an exhaustive list, it does reflect the superb coke inhibition property of our Ni-

SiO<sub>2</sub>@CeO<sub>2</sub> catalyst while maintaining a high dry reforming activity.

### 3.3.4. XANES analysis

To investigate the change in the Ni oxidation state before and after

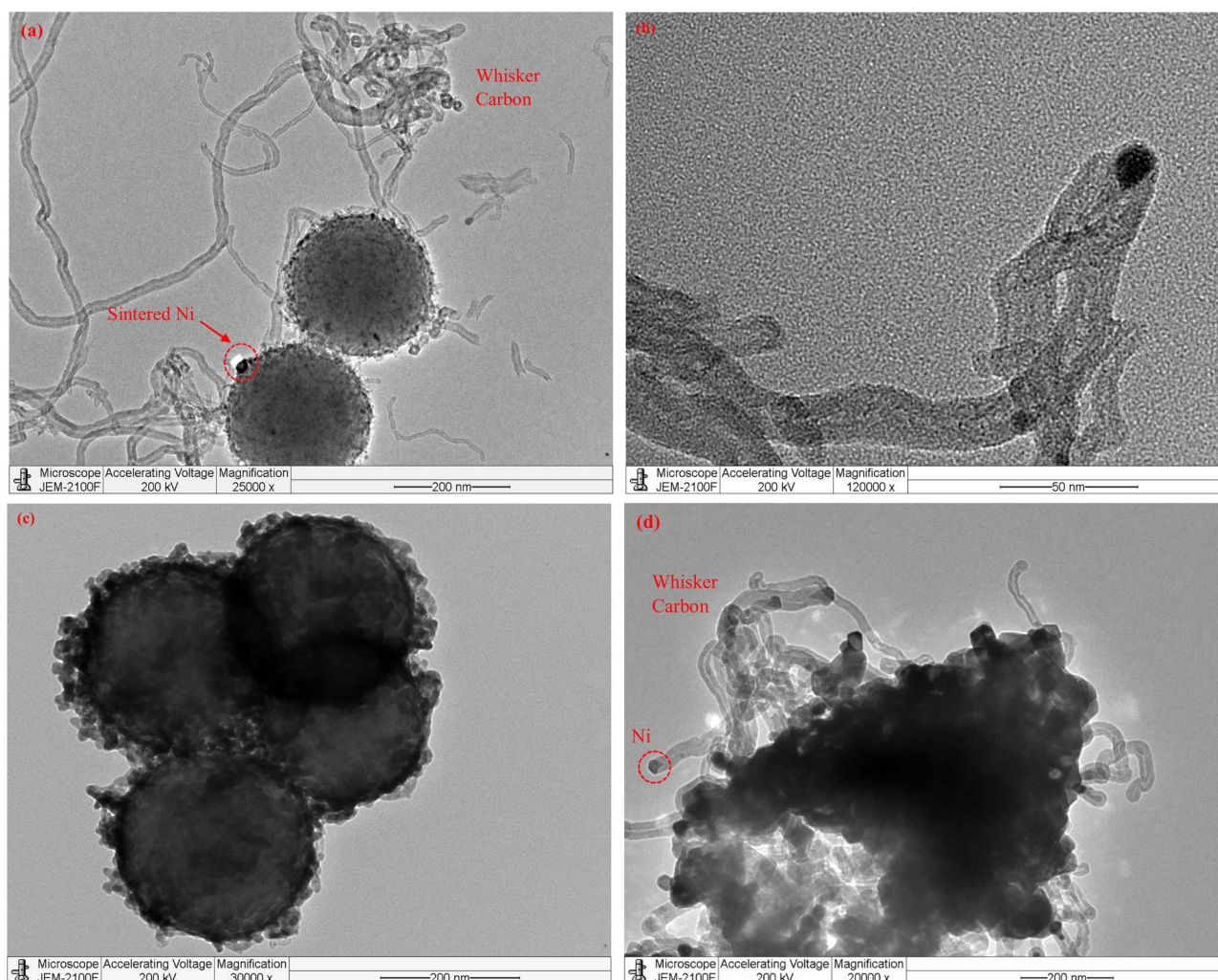


**Fig. 10.** TEM Micrograph of spent catalyst. (a) Ni-SiO<sub>2</sub> after 22 h, (b) Magnified image for filamentous carbon formed on spent Ni-SiO<sub>2</sub> showing Ni metal at the tip, (c) Spent Ni-SiO<sub>2</sub>@CeO<sub>2</sub> after 72 h reaction, (d) Spent Ni-CeO<sub>2</sub> after 72 h reaction.

reaction, XANES analysis was done on all three catalysts after reduction and after 6 h of bio-gas reforming reaction. The XANES signals from the measured absorption spectra were extracted by the pre-edge background and were normalized by dividing the peak intensity by the height of the absorption edge. The data reduction was done using the Athena software program.

Fig. 11a shows the XANES spectra for the Ni-K absorption edge for Ni foil (Ni<sup>0</sup>) and NiO (Ni<sup>2+</sup>) and Fig. 11b–d shows the Ni-K absorption edge for the reduced and spent Ni-SiO<sub>2</sub>, Ni-SiO<sub>2</sub>@CeO<sub>2</sub> and Ni-CeO<sub>2</sub> catalysts respectively. The XANES spectra for nickel in oxidized state Ni<sup>2+</sup> shows a pre-edge peak, and a white line is observed at 8350.2 eV. For metallic Ni<sup>0</sup>, the spectrum shows a weaker pre-edge peak and no white line [68]. For the reduced Ni-SiO<sub>2</sub> catalyst, the XANES spectrum shows a small white line intensity, showing that Ni is not completely reduced to metallic state, in line with TPR results (Table 1). The spent Ni-SiO<sub>2</sub> catalyst shows a similar white line intensity and a slightly stronger pre-edge peak, indicating it is slightly more oxidized than the reduced catalyst. The spectrum for the freshly reduced Ni-SiO<sub>2</sub>@CeO<sub>2</sub> catalyst shows Ni in completely reduced state. The spent Ni-SiO<sub>2</sub>@CeO<sub>2</sub> spectrum, however, shows a clear increase in the white line intensity compared to the freshly reduced catalyst, showing that the Ni is partly surface oxidized [68]. It is likely that the ceria in the Ni-SiO<sub>2</sub>@CeO<sub>2</sub> catalyst aids in the gradual surface oxidation of nickel by activating CO<sub>2</sub> by means of its oxygen vacancies and providing oxygen species for Ni oxidation. This partial oxidation of Ni may explain the gradual

reduction in activity for the Ni-SiO<sub>2</sub>@CeO<sub>2</sub> catalyst as shown in Fig. 7.

Interestingly, for the impregnated Ni-CeO<sub>2</sub> catalyst, such an oxidation of Ni is not observed. This may be explained by the lower amount of oxygen vacancies in Ni-CeO<sub>2</sub> as compared to Ni-SiO<sub>2</sub>@CeO<sub>2</sub>, as shown by XPS measurements on the reduced catalysts (Section 3.1.5). Also, the nickel particle size is much bigger in Ni-CeO<sub>2</sub> than Ni-SiO<sub>2</sub>@CeO<sub>2</sub>, making it less susceptible to oxidation at the nickel–ceria interface.

### 3.4. In-situ DRIFTS analysis

#### 3.4.1. In-situ DRIFTS analysis on Ni-SiO<sub>2</sub>

In-situ DRIFTS analysis was conducted to identify the intermediate species formed on the catalyst surface during reaction and to understand the reaction mechanism. DRIFTS results were recorded by introducing a continuous flow of CH<sub>4</sub> and CO<sub>2</sub> diluted with Helium to the reduced catalyst in an FTIR cell. Prior to introducing reactant gases, the catalyst was reduced *ex-situ* at 800 °C for 1 h and then *in-situ* at 600 °C for 30 min in a hydrogen flow of 30 ml/min followed by purging with Helium.

The DRIFTS spectrum of Ni-SiO<sub>2</sub> (Fig. 12a) shows peaks at 3015, 1304 cm<sup>-1</sup> and 2360, 2340 cm<sup>-1</sup> for gas phase CH<sub>4</sub> and CO<sub>2</sub> respectively. The gas phase CO peak appearing as a doublet at 2170 and 2130 cm<sup>-1</sup> gets stronger with increasing temperature, indicating increasing conversion of methane and carbon dioxide. A strong peak

**Table 3**

Activity and Coke-resistance of Ni-SiO<sub>2</sub>@CeO<sub>2</sub> catalyst compared to recently published catalysts for dry reforming of methane (emphasis has been given to recent and low temperature studies).

Catalyst	Reaction Conditions	Methane conversion activity (for selected catalyst)	Coke Deposition	Ref.
Ni-SiO <sub>2</sub> @CeO <sub>2</sub>	600 °C, CH <sub>4</sub> /CO <sub>2</sub> = 3:2 GHSV = 200,000 h <sup>-1</sup> , TOS = 72 h	0.12 mol CH <sub>4</sub> min <sup>-1</sup> g metal <sup>-1</sup>	Not detected	This work
SiO <sub>2</sub> supported Ni catalysts				
Ni-SiO <sub>2</sub> (Reduction- Oxidation- Reduction pretreated)	600 °C, CH <sub>4</sub> /CO <sub>2</sub> /N <sub>2</sub> = 1:1:1 GHSV = 144,000 ml/h g, TOS = 12 h	0.114 mol CH <sub>4</sub> min <sup>-1</sup> g metal <sup>-1</sup> declines by 80% in 12 h (10% Ni-SiO <sub>2</sub> ROR)	18 mg Carbon/ L CH <sub>4</sub> converted	[59]
Ni-phylosilicate @SiO <sub>2</sub>	600 °C, CH <sub>4</sub> /CO <sub>2</sub> /He = 1:1:1 GHSV = 60,000 ml/h g, TOS = 24 h	0.21 mol CH <sub>4</sub> min <sup>-1</sup> g metal <sup>-1</sup> (NiPS@SiO <sub>2</sub> -0.4)	7.6% weight loss in TGA for spent catalyst	[23]
Ni/ MCM-41	600 °C, CH <sub>4</sub> /CO <sub>2</sub> /Ar = 1:1:1 GHSV = 36,000 ml/h g, TOS = 4 h	0.015 mol CH <sub>4</sub> min <sup>-1</sup> g metal <sup>-1</sup> (0.5Ru@Ni/ MCM-41)	~70% weight loss in TGA for spent catalyst	[58]
Ni@SiO <sub>2</sub> yolk-shell	700 °C, CH <sub>4</sub> /CO <sub>2</sub> /N <sub>2</sub> = 1:1:1 GHSV = 36,000 ml/h g, TOS = 50 h	0.55 mol CH <sub>4</sub> min <sup>-1</sup> g metal <sup>-1</sup> (Ni yolk@Ni@ SiO <sub>2</sub> 12 h treatment)	1.4% carbon after 20 h reaction	[55]
Ni@SiO <sub>2</sub>	750 °C, CH <sub>4</sub> /CO <sub>2</sub> /N <sub>2</sub> = 1:1:2 GHSV = 48,000 ml/h g, TOS = 25 h	0.017 mol CH <sub>4</sub> min <sup>-1</sup> g metal <sup>-1</sup>	0.012 g coke/ g catalyst.	[63]
Ni-Mg Phyllosilicate nanotube @ SiO <sub>2</sub>	750 °C, CH <sub>4</sub> /CO <sub>2</sub> /He = 1:1:1 GHSV = 60,000 ml/h g, TOS = 72 h	0.109 mol CH <sub>4</sub> min <sup>-1</sup> g metal <sup>-1</sup> (NiMg-Phyllosilicate @SiO <sub>2</sub> )	Not detected	[64]
Ni/SiO <sub>2</sub> @SiO <sub>2</sub>	800 °C, CH <sub>4</sub> /CO <sub>2</sub> /N <sub>2</sub> = 9:9:2 GHSV = 12,000 ml/h g, TOS = 100 h	0.502 mol CH <sub>4</sub> min <sup>-1</sup> g metal <sup>-1</sup> (5.2 nm Ni/ SiO <sub>2</sub> @SiO <sub>2</sub> )	No coke detected in TPO.	[66]
CeO <sub>2</sub> supported Ni catalyst				
Mesoporous Ni/Ce <sub>1-x</sub> Ni <sub>x</sub> O <sub>2-y</sub>	700 °C, CH <sub>4</sub> /CO <sub>2</sub> = 1:1 GHSV = 12,000 ml/h g, TOS = 40 h	0.027 mol CH <sub>4</sub> min <sup>-1</sup> g metal <sup>-1</sup> (Ni/mp-Ce <sub>1-x</sub> Ni <sub>x</sub> O <sub>2-y</sub> )	~10% weight loss in TGA for spent catalyst	[67]
Ce doped Ni-SBA-16	700 °C, CH <sub>4</sub> /CO <sub>2</sub> /He = 1:1:1 GHSV = 45,000 ml/h g, TOS = 100 h	0.16 molCH <sub>4</sub> min <sup>-1</sup> g metal <sup>-1</sup> (NiCe/SBA-16)	3.8% coke	[20]
Ni-Co/ CeZrO <sub>2</sub>	750 °C, CH <sub>4</sub> /CO <sub>2</sub> = 3:2 GHSV = 12,000 ml/h g, TOS = 80 h	0.098 molCH <sub>4</sub> min <sup>-1</sup> g metal <sup>-1</sup> (CeZr 3EG)	5.7 % coke	[5]
Ag promoted Ni-CeO <sub>2</sub>	750 °C, CH <sub>4</sub> /CO <sub>2</sub> /N <sub>2</sub> = 25:25:18 GHSV = 13,400 h <sup>-1</sup> , TOS = 100 h	0.023 mol CH <sub>4</sub> min <sup>-1</sup> g metal <sup>-1</sup> (Ni/CeO <sub>2</sub> -3 Ag)	0.251% coke	[65]
Other Ni- based catalysts				
Zr promoted (Mg, Ni, Al) O	550 °C, CH <sub>4</sub> /CO <sub>2</sub> /Ar = 1:1:8 GHSV = 20,000 h <sup>-1</sup> , TOS = 5 h	0.0017 mol CH <sub>4</sub> min <sup>-1</sup> g metal <sup>-1</sup> (HNiZr3)	12.7% weight loss in TGA for spent catalyst	[57]
La promoted Ni-Mg-Al (hydrotalcite derived)	550 °C, CH <sub>4</sub> /CO <sub>2</sub> /Ar = 1:1:8 GHSV = 20,000 h <sup>-1</sup> , TOS = 8.3 h	0.0004 mol CH <sub>4</sub> min <sup>-1</sup> ml catalyst <sup>-1</sup> (NiLaMgAl – HN3)	~87.5% weight loss in TGA for spent catalyst	[56]
Ni-Co/ Mesoporous Al <sub>2</sub> O <sub>3</sub>	600 °C, CH <sub>4</sub> /CO <sub>2</sub> /Ar = 1:1:1 GHSV = 36,000 ml/h g, TOS = 4 h	0.053 mol CH <sub>4</sub> min <sup>-1</sup> g metal <sup>-1</sup> (2.5Co-2.5Ni@ SGA)	~12% weight loss in TGA for spent catalyst	[60]
Mg/ Ca promoted Co-Ni ordered mesoporous material	700 °C, CH <sub>4</sub> /CO <sub>2</sub> = 1:1 GHSV = 15,000 ml/h g, TOS = 100 h	0.058 mol CH <sub>4</sub> min <sup>-1</sup> g metal <sup>-1</sup> (OMA-5Co5Ni3Ca)	6 % weight loss in TGA for spent catalyst	[61]
Ni-La <sub>2</sub> O <sub>3</sub> nanorod	700 °C, CH <sub>4</sub> /CO <sub>2</sub> /N <sub>2</sub> = 3:3:14 GHSV = 60,000 ml/h g, TOS = 50 h	0.082 mol CH <sub>4</sub> min <sup>-1</sup> g metal <sup>-1</sup> (5Ni/La <sub>2</sub> O <sub>3</sub> -LOC)	10.3 % weight loss in TGA for spent catalyst	[62]

observed at 2040 cm<sup>-1</sup> is attributed to linearly adsorbed CO on Ni while the weaker peaks at 1930 and 1800 cm<sup>-1</sup> are assigned to bridged and multi-centred CO on Ni [69,70]. The linearly adsorbed CO peak stays strong even at 600 °C, suggesting that it is an active intermediate in the reaction. Peaks are also observed in the 3500–3800 cm<sup>-1</sup> range which may be attributed to O–H stretching of hydroxyl groups on the unreduced Ni-phylosilicate surface.

The observed spectra agree with the reported mono-functional pathway for DRM on SiO<sub>2</sub> supported metal catalysts where both the CH<sub>4</sub> and CO<sub>2</sub> are activated on the metal [71,72], with the inert SiO<sub>2</sub> support playing no direct role in the reaction. CH<sub>4</sub> adsorbs on a Ni site in a dissociative manner to form H<sub>2</sub> and adsorbed carbon either directly or *via* intermediates like CH<sub>x</sub>. CO<sub>2</sub> adsorbs on Ni and can dissociate to form CO and adsorbed O, and the adsorbed Ni-O species subsequently reacts with Ni-C produced from methane decomposition to form another molecule of CO. The schematic for the reaction mechanism on Ni-SiO<sub>2</sub> catalyst is shown in Scheme 2(a).

### 3.4.2. In-situ DRIFTS analysis on Ni-SiO<sub>2</sub>@CeO<sub>2</sub>

The DRIFTS spectrum for the Ni-SiO<sub>2</sub>@CeO<sub>2</sub> catalyst under DRM conditions (Fig. 12b) shows a broad peak around 1400–1550 cm<sup>-1</sup> assigned to carbonate species on CeO<sub>2</sub> along with gas phase CO<sub>2</sub>, CH<sub>4</sub> and CO peaks. A distinct feature of the DRIFTS spectrum of the Ni-SiO<sub>2</sub>@CeO<sub>2</sub> catalyst is the absence of linearly adsorbed carbonyl species on Ni. At higher temperatures, peaks are observed at 1930 and 1804 cm<sup>-1</sup> characteristic of bridging carbonyl groups. The absence of linearly adsorbed CO on the Ni-SiO<sub>2</sub>@CeO<sub>2</sub> suggests that the presence of ceria, especially on the Ni surface, either modifies the surface properties of Ni, making it unable to adsorb CO and/or changes the reaction mechanism where the formation of adsorbed CO on Ni is no longer a major intermediate. Either way, this phenomenon can directly inhibit coke formation from the Boudouard reaction Eq. (3) by reducing the concentration of adsorbed CO on Ni.

To get a better insight into the reaction mechanism, we conducted DRIFTS analysis by alternately pulsing CH<sub>4</sub> and CO<sub>2</sub> streams on the

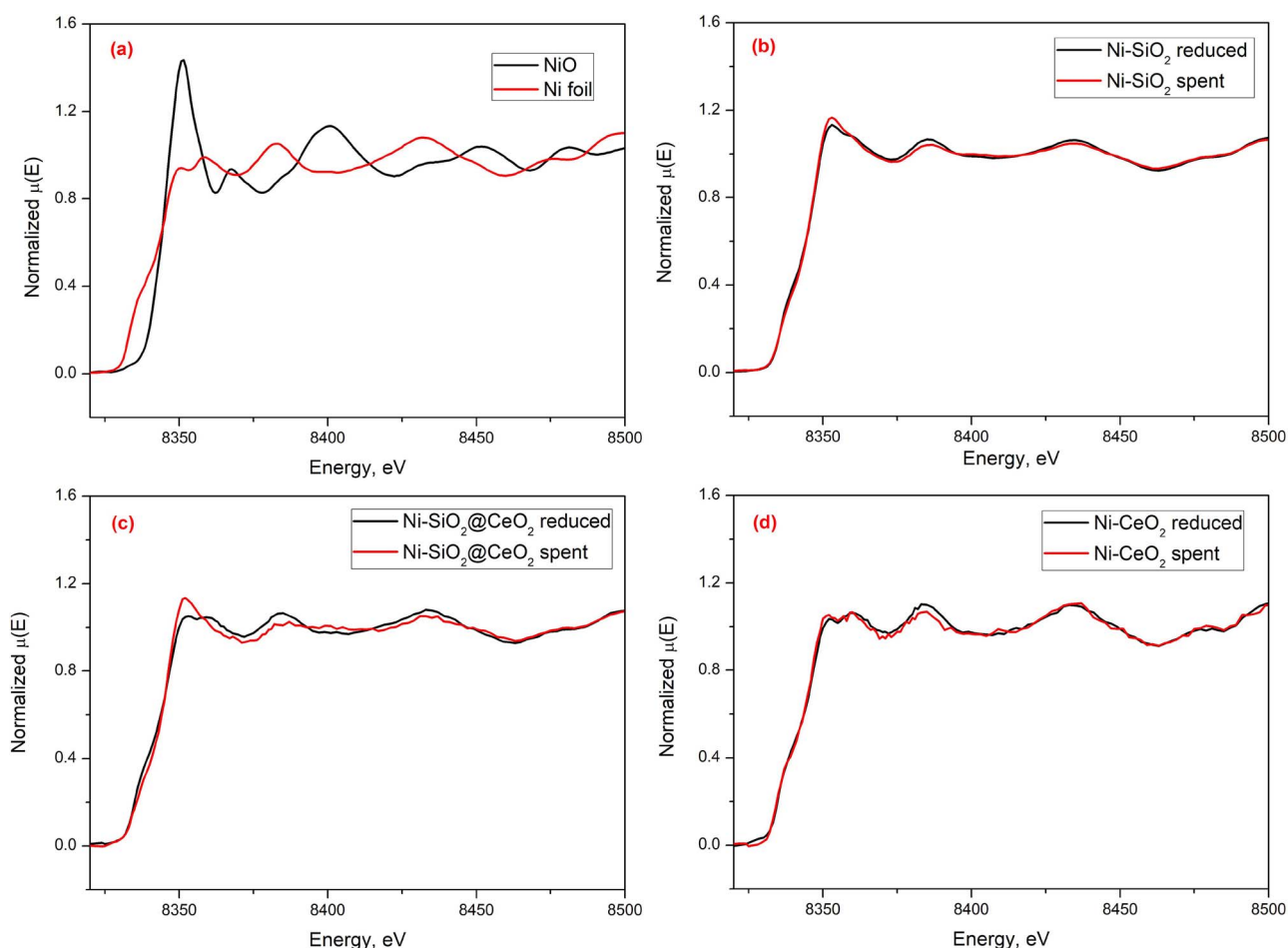


Fig. 11. XANES Ni K-edge spectra for (a)  $\text{Ni}^0$  and  $\text{NiO}$  standard, (b) freshly reduced and spent  $\text{Ni-SiO}_2$ , (c) freshly reduced and spent  $\text{Ni-SiO}_2@ \text{CeO}_2$ , and (d) freshly reduced and spent  $\text{Ni-CeO}_2$ .

catalyst at 500 °C. The catalyst is first reduced under hydrogen flow followed by helium purging. A methane pulse is then introduced, and the transient spectra is recorded with time (Fig. 13a). It is interesting to note that apart from the gas phase  $\text{CH}_4$  peaks, we can also observe weak gas phase  $\text{CO}_2$  peaks at  $2360\text{ cm}^{-1}$  and a broad peak in the range of  $1400\text{--}1500\text{ cm}^{-1}$  for carbonates. Since methane is the only gas introduced, the presence of carbonates and  $\text{CO}_2$  peaks suggest that the lattice oxygen of ceria is able to oxidize the carbon species formed from methane decomposition. Toyir et al. also made a similar observation where a temperature programmed reduction of  $\text{Ir/CeO}_2$  catalyst under  $\text{CH}_4$  yielded  $\text{CO}$ ,  $\text{CO}_2$  and  $\text{H}_2$  due to the reduction of  $\text{Ce}^{4+}$  into  $\text{Ce}^{3+}$  [73]. The ability of ceria to oxidize methane in the absence of  $\text{CO}_2$  is of high significance to the coke resistance property of the  $\text{Ni-SiO}_2@ \text{CeO}_2$  catalyst.

Apart from carbonates, peaks are also observed at  $1345$  and  $2800\text{--}2900\text{ cm}^{-1}$ , indicating the formation of formate species [74]. The methane pulse is followed by a  $\text{CO}_2$  pulse where the spectrum shows an increase in the carbonate peaks and  $-\text{OH}$  peaks. In a subsequent methane pulse, no change in the carbonate peak intensity is observed on introducing the methane pulse, which indicates that the carbonates may not be an active intermediate in this case but are rather a spectator species [75].

Based on the absence of the linearly adsorbed  $\text{CO}$  peaks on the  $\text{Ni-SiO}_2@ \text{CeO}_2$  catalyst (Fig. 12b) and the ability of the lattice oxygen in ceria to oxidize carbon (Fig. 13), we infer that the dry reforming reaction over this catalyst happens via a bi-functional redox mechanism with the ceria lattice oxygen playing an active role in carbon conversion [4]. Methane undergoes dissociative adsorption on  $\text{Ni}$  to form  $\text{C-Ni}$

which is converted by the oxygen sites  $\text{O}_x$  on ceria at the  $\text{Ni-CeO}_2$  interface to form  $\text{CO}$  and an oxygen vacancy  $\text{O}_{x-1}$ . The oxygen vacancies created on  $\text{CeO}_2$  act as adsorption and activation sites for  $\text{CO}_2$  which readily dissociates to form  $\text{CO}$  and regenerates the  $\text{O}_x$ . Due to the high mobility of lattice oxygen of ceria, the  $\text{O}_x$  species can diffuse very fast from the bulk to the  $\text{Ni-CeO}_2$  interface where it is consumed. The schematic for the bi-functional mechanism on  $\text{Ni-SiO}_2@ \text{CeO}_2$  catalyst is shown in Scheme 2(b).

Since  $\text{CO}_2$  is dissociated on sites on the ceria support and not on  $\text{Ni}$  surface, adsorbed  $\text{Ni-CO}$  species formed by  $\text{CO}_2$  dissociation is not formed on the  $\text{Ni-SiO}_2@ \text{CeO}_2$  catalyst. This can explain why the intensity of the adsorbed  $\text{CO}$  on  $\text{Ni}$  peak for the  $\text{Ni-SiO}_2@ \text{CeO}_2$  catalyst is much lower than the  $\text{Ni-SiO}_2$  catalyst, where  $\text{CO}_2$  dissociation occurs on  $\text{Ni}$  surface.

#### 3.4.3. In-situ DRIFTS analysis on $\text{Ni-CeO}_2$

The DRIFTS spectra for  $\text{Ni-CeO}_2$  is shown in Fig. 12c and is similar to that of  $\text{Ni-SiO}_2@ \text{CeO}_2$ . Gas phase peaks for  $\text{CH}_4$  at  $3015$ ,  $1304\text{ cm}^{-1}$ ,  $\text{CO}_2$  at  $2360$ ,  $2340\text{ cm}^{-1}$  and  $\text{CO}$  product at  $2170$  and  $2130\text{ cm}^{-1}$  are observed. The gas phase  $\text{CO}$  peaks for  $\text{Ni-CeO}_2$  start appearing at slightly higher temperature compared to  $\text{Ni-SiO}_2@ \text{CeO}_2$ , which is consistent with the lower activity of  $\text{Ni-CeO}_2$ . Carbonate and formate species are observed at  $1400\text{--}1600\text{ cm}^{-1}$  and  $1345\text{ cm}^{-1}$  respectively. Similar to  $\text{Ni-SiO}_2@ \text{CeO}_2$ , no peak is observed for  $\text{CO}$  adsorbed on  $\text{Ni}$ , which indicates that the same bi-functional redox mechanism is followed in  $\text{Ni-CeO}_2$ , as is expected. The carbonate peaks are much weaker in  $\text{Ni-CeO}_2$  compared to  $\text{Ni-SiO}_2@ \text{CeO}_2$ , which is possibly because of higher oxygen vacancies in  $\text{Ni-SiO}_2@ \text{CeO}_2$  making  $\text{CO}_2$  absorption

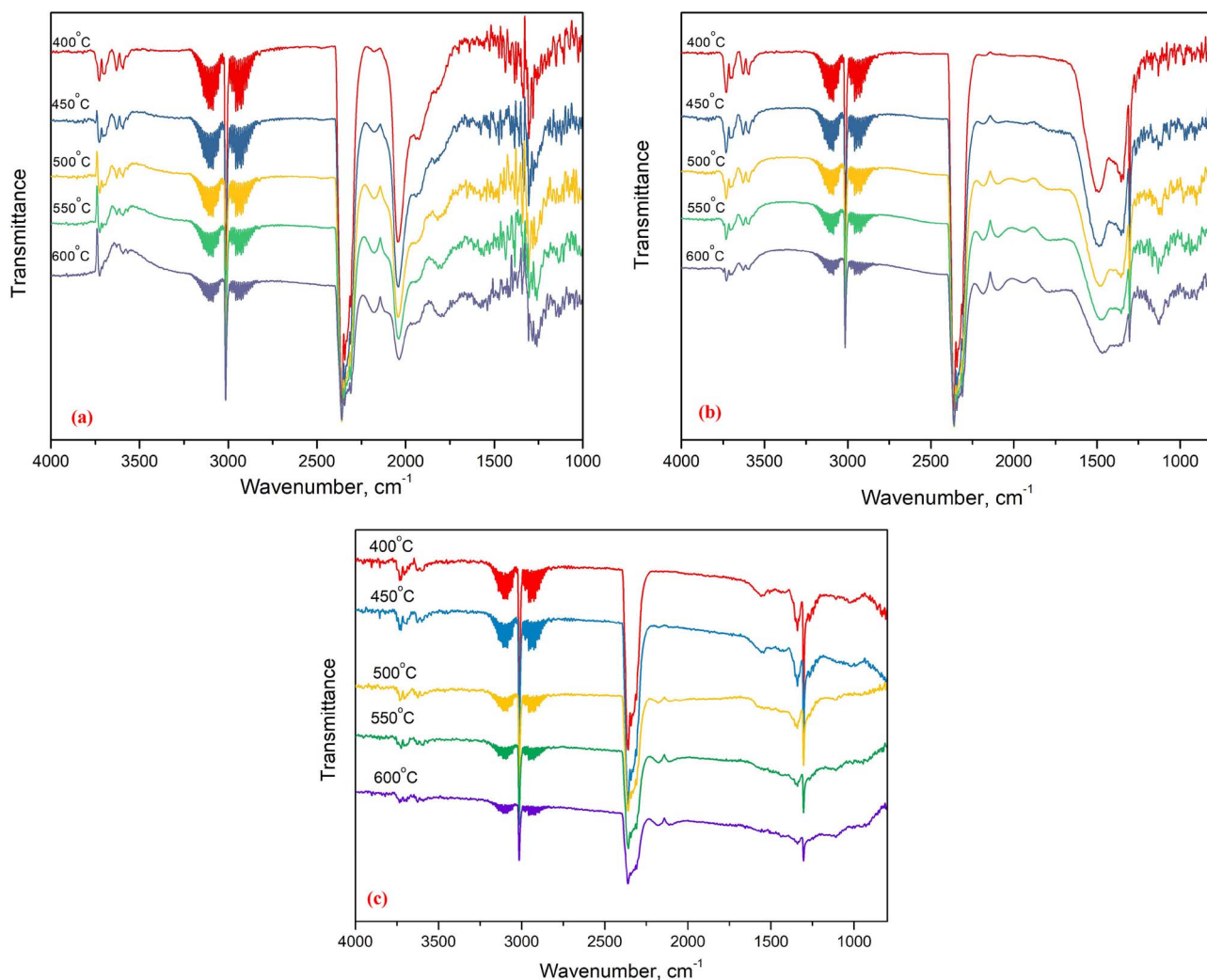
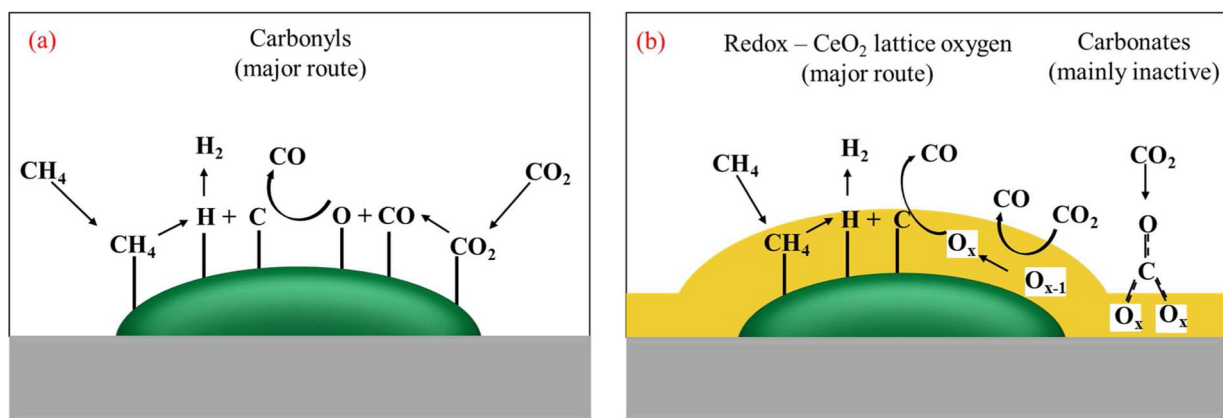


Fig. 12. DRIFTS spectra obtained during dry reforming of methane on (a) Ni-SiO<sub>2</sub>, (b) Ni-SiO<sub>2</sub>@CeO<sub>2</sub> & (c) Ni-CeO<sub>2</sub> at 400 °C–600 °C (CH<sub>4</sub>/CO<sub>2</sub>/He = 2/2/20 ml/min).



Scheme 2. Mono-functional and Bi-functional reaction mechanism for methane dry reforming on (a) Ni-SiO<sub>2</sub> and (b) Ni-SiO<sub>2</sub>@CeO<sub>2</sub> catalyst, respectively.

stronger.

Thus, from the DRIFTS analysis on the Ni-SiO<sub>2</sub>, Ni-SiO<sub>2</sub>@CeO<sub>2</sub> and Ni-CeO<sub>2</sub> catalysts, we propose that the ceria shell causes a change of the dry reforming mechanism from a mono-functional to bi-functional pathway involving active sites on ceria in the Ni-SiO<sub>2</sub>@CeO<sub>2</sub> catalyst. The absence of adsorbed CO on Ni on the Ni-SiO<sub>2</sub>@CeO<sub>2</sub> and Ni-CeO<sub>2</sub> catalyst provides evidence supporting the bi-functional mechanism. The close interaction of Ni and ceria, as evidenced by TPR, H<sub>2</sub>

Chemisorption and HRTEM results for the Ni-SiO<sub>2</sub>@CeO<sub>2</sub> catalyst also indicate that there is sufficient Ni-CeO<sub>2</sub> interface which can cause this change in mechanism.

### 3.5. Discussion – superior coke-resistance of Ni-SiO<sub>2</sub>@CeO<sub>2</sub>

To understand the factors behind the high coke inhibition property of Ni-SiO<sub>2</sub>@CeO<sub>2</sub> catalyst, it is first important to look at the product

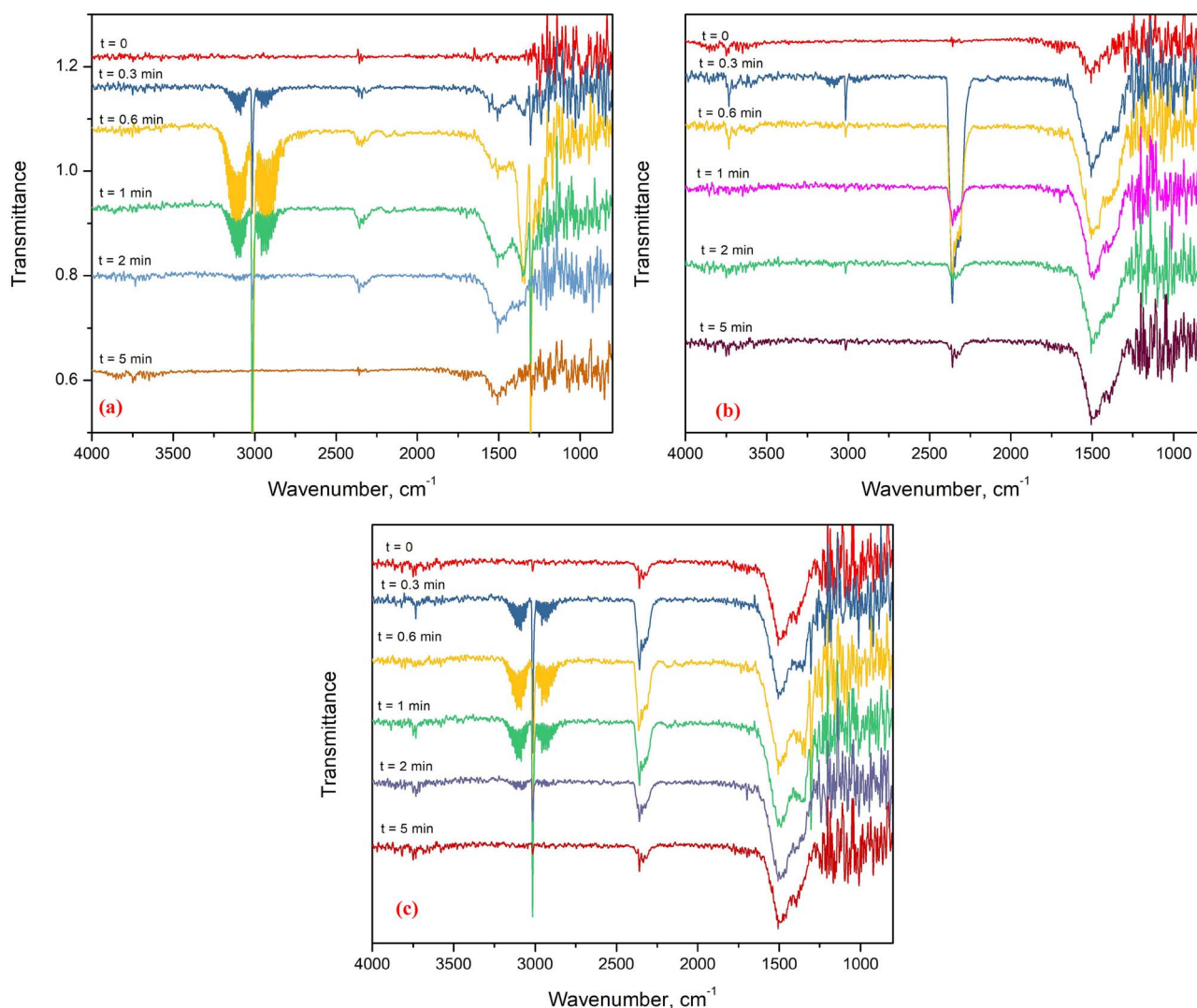


Fig. 13. DRIFTS spectra obtained for Ni-SiO<sub>2</sub>@CeO<sub>2</sub> under alternate pulses of CH<sub>4</sub> and CO<sub>2</sub> at 500 °C. (a) First CH<sub>4</sub> pulse after *in-situ* reduction and 1-h long He purge, (b) subsequent CO<sub>2</sub> pulse, (c) subsequent CH<sub>4</sub> pulse.

distribution over the different catalysts. From the H<sub>2</sub>/CO ratio during biogas reforming over the three catalysts at 600 °C (Section 3.2.1), it is clear that the reverse water gas shift reaction and water formation is favoured on the ceria containing catalysts. The water formation rate per mole methane converted increases in the sequence Ni-SiO<sub>2</sub> (~0.75 mol H<sub>2</sub>O/mol CH<sub>4</sub>) < Ni-SiO<sub>2</sub>@CeO<sub>2</sub> (~0.88 mol H<sub>2</sub>O/mol CH<sub>4</sub>) < Ni-CeO<sub>2</sub> (~1 mol H<sub>2</sub>O/mol CH<sub>4</sub>) (refer Fig. S7 in Supplementary information). Steam being a stronger oxidant than CO<sub>2</sub> helps in easier coke removal during reforming reaction and hence, the higher water formation may be a factor in the reduced coke formation on the core-shell Ni-SiO<sub>2</sub>@CeO<sub>2</sub> catalyst.

In order to investigate the effect of the higher water formation on Ni-SiO<sub>2</sub>@CeO<sub>2</sub> on its coke formation as compared to Ni-SiO<sub>2</sub>, dry reforming of biogas was conducted on Ni-SiO<sub>2</sub> with the external addition of water. Keeping all other conditions same as the stability test in Section 3.2.2, 0.045 mols min<sup>-1</sup> g<sub>Ni</sub><sup>-1</sup> of water were introduced into the reaction feed to Ni-SiO<sub>2</sub> catalyst, to make up for the difference in water formed on Ni-SiO<sub>2</sub> and Ni-SiO<sub>2</sub>@CeO<sub>2</sub>. TGA was performed on the spent catalyst after 15 h of reaction at 600 °C (Fig. S9). The TGA curve shows a weight loss of 33% or 0.49 coke/g<sub>cat</sub>. The amount of coke formed is lower than that in the run with no additional water feed but is still much higher than that of Ni-SiO<sub>2</sub>@CeO<sub>2</sub> (Section 3.3.1). This result shows that while the higher water production in Ni-SiO<sub>2</sub>@CeO<sub>2</sub> does play a role in reducing coke formation, there are other factors that lead

to the excellent coke resistance in Ni-SiO<sub>2</sub>@CeO<sub>2</sub>.

The excellent stability and coke inhibition properties of the Ni-SiO<sub>2</sub>@CeO<sub>2</sub> catalyst is caused by two other factors: the confinement effect of the ceria shell on the nickel nanoparticles and the strong redox ability of ceria.

In our Ni-SiO<sub>2</sub>@CeO<sub>2</sub> catalyst, the Ni particles are encapsulated between the silica support and the CeO<sub>2</sub> shell, which provides a dual confinement effect on the Ni particles. Using a Ni phyllosilicate precursor to form Ni-SiO<sub>2</sub> itself provides the first confinement as decomposition of the phyllosilicate structure during reduction produces uniform and small Ni nanoparticles embedded in SiO<sub>2</sub> with strong metal support interaction. However, under the current dry reforming conditions, this partial encapsulation in the SiO<sub>2</sub> matrix is not enough to prevent Ni sintering. TEM images of the spent Ni-SiO<sub>2</sub> catalyst (Figs. 10a,b, S8a) clearly show the presence of agglomerated Ni particles after the reaction. In the Ni-SiO<sub>2</sub>@CeO<sub>2</sub> catalyst, the CeO<sub>2</sub> layer provides another layer of encapsulation and protects the particles from sintering. HRTEM and XRD analysis of the spent Ni-SiO<sub>2</sub>@CeO<sub>2</sub> catalyst (Section 3.3) shows that there is very low sintering and the average Ni particle size remains less than 6 nm even after 72 h of reaction. Additionally, the presence of the encapsulating CeO<sub>2</sub> provides a steric inhibition to the growth of carbon whiskers that are the primary form of carbon on the spent Ni-SiO<sub>2</sub> catalyst and cause the uprooting of Ni nanoparticles from the silica support. From Fig. 10(c), we can see that

the CeO<sub>2</sub> shell has inhibited the growth of filamentous carbon around the active Ni centre.

The redox property of the CeO<sub>2</sub> shell is the other and probably the more important factor in the high coke inhibition property of the Ni-SiO<sub>2</sub>@CeO<sub>2</sub> catalyst. It is well-known that CeO<sub>2</sub> can undergo substantial oxygen stoichiometric changes by switching between Ce<sup>4+</sup> and Ce<sup>3+</sup>, which creates a high concentration of highly mobile oxygen vacancies that act as source or sink for oxygen involved in reactions on ceria surface [4]. CeO<sub>2</sub> can thus promote the dissociation of CO<sub>2</sub> to form mobile oxygen species that can oxidize the active carbon formed on Ni during reforming, preventing the growth or accumulation of inactive carbonaceous deposits. For the participation of CeO<sub>2</sub> in carbon gasification, it is however essential that all the Ni particles are in close contact with CeO<sub>2</sub>. That is why we have used a thin Ni-phyllsilicate layer supported on silica as the core instead of a homogeneous Ni-phyllsilicate core which could prevent interaction of the outer ceria layer with the inner core nickel particles. The TPR, XRD and TEM analysis of the fresh Ni-SiO<sub>2</sub>@CeO<sub>2</sub> catalysts indicate good interaction between Ni and CeO<sub>2</sub>. From *in-situ* DRIFTS analysis, we observe that the ceria shell has altered the entire reaction mechanism for DRM from a monofunctional pathway on Ni-SiO<sub>2</sub> to a bi-functional mechanism in Ni-SiO<sub>2</sub>@CeO<sub>2</sub> where the ceria also actively participates in the reaction by continuously providing lattice oxygen. This bi-functional mechanism is likely a major reason for the higher stability and coke-inhibition properties of the Ni-SiO<sub>2</sub>@CeO<sub>2</sub> catalyst.

Ni-CeO<sub>2</sub> catalyst also possesses much higher stability and coke-resistance than Ni-SiO<sub>2</sub> because of the availability of oxygen species in CeO<sub>2</sub>. However, CeO<sub>2</sub> by itself has poor thermal stability and sinters easily at high temperatures [76]. The Ni/CeO<sub>2</sub> catalyst suffers from poor Ni dispersion and sintering at dry reforming conditions, leading to poor activity [43,44]. The large Ni particle size also results in the formation of some whisker carbon during dry reforming.

#### 4. Conclusion

A novel core-shell structured Ni-SiO<sub>2</sub>@CeO<sub>2</sub> catalyst with Ni nanoparticles sandwiched between SiO<sub>2</sub> and CeO<sub>2</sub> layers was synthesized and applied for dry reforming of bio-gas (CH<sub>4</sub>/CO<sub>2</sub> = 1.5) at low temperature (600 °C). The Ni-SiO<sub>2</sub>@CeO<sub>2</sub> catalyst showed negligible coke formation over a 72 h stability test while maintaining high dry reforming activity (~0.12 mol CH<sub>4</sub> min<sup>-1</sup> gNi<sup>-1</sup>). In comparison, a Ni-SiO<sub>2</sub> catalyst without the CeO<sub>2</sub> coating showed low activity (~0.08 mol CH<sub>4</sub> min<sup>-1</sup> gNi<sup>-1</sup>) and extensive coke formation (1.39 gC/g<sub>catalyst</sub>) that blocked the reactor within 22 h, while a Ni-CeO<sub>2</sub> catalyst demonstrated stable performance for 72 h but at very low activity (~0.04 mol CH<sub>4</sub> min<sup>-1</sup> gNi<sup>-1</sup>) and higher coke formation than Ni-SiO<sub>2</sub>@CeO<sub>2</sub> (0.047 gC/g<sub>catalyst</sub>). The higher activity of the Ni-SiO<sub>2</sub>@CeO<sub>2</sub> catalyst is attributed primarily to the higher Ni dispersion on Ni-SiO<sub>2</sub>@CeO<sub>2</sub>.

The high coke resistance of the sandwiched core-shell catalyst is due to the dual confinement effect provided by the encapsulation of Ni nanoparticles between SiO<sub>2</sub> and CeO<sub>2</sub>, the redox capacity of the ceria shell and higher RWGS activity of ceria. The confinement effect of the core-shell structure prevents Ni sintering and is the primary reason for higher coke resistance of Ni-SiO<sub>2</sub>@CeO<sub>2</sub> than Ni-CeO<sub>2</sub>. When compared to the Ni-SiO<sub>2</sub> catalyst, the redox nature of the ceria shell also contributes heavily to the higher coke-resistance of Ni-SiO<sub>2</sub>@CeO<sub>2</sub>. *In-situ* DRIFTS on the pristine Ni-SiO<sub>2</sub> and Ni-SiO<sub>2</sub>@CeO<sub>2</sub> catalysts show a clear difference in intermediate species which indicate that the CeO<sub>2</sub> shell participates in the dry reforming reaction by supplying oxygen species, thus reducing coke accumulation.

#### Acknowledgements

The authors gratefully thank National University of Singapore, National Research Foundation, Prime Minister's Office, Singapore and the National Environment Agency under the Waste-to-Energy

Competitive Research Program (WTE CRP 1501 103) and Agency for Science, Technology & Research (AME IRG Grant no R-279-000-509-305) for generously supporting this work.

#### Appendix A. Supplementary data

Supplementary material related to this article can be found, in the online version, at doi:<https://doi.org/10.1016/j.apcatb.2018.02.041>.

#### References

- [1] Z. Bian, S. Das, M.H. Wai, P. Hongmanom, S. Kawi, A review on bimetallic nickel-based catalysts for CO<sub>2</sub> reforming of methane, *ChemPhysChem* 18 (2017) 1–19.
- [2] S. Kawi, Y. Kathiraser, J. Ni, U. Oemar, Z. Li, E.T. Saw, Progress in synthesis of highly active and stable nickel-based catalysts for carbon dioxide reforming of methane, *ChemSusChem* 8 (21) (2015) 3556–3575.
- [3] Y. Kathiraser, U. Oemar, E.T. Saw, Z. Li, S. Kawi, Kinetic and mechanistic aspects for CO<sub>2</sub> reforming of methane over Ni based catalysts, *Chem. Eng. J.* 278 (2015) 62–78.
- [4] N. Laosiripojana, W. Sutthisripok, S. Assabumrungrat, Synthesis gas production from dry reforming of methane over CeO<sub>2</sub> doped Ni/Al<sub>2</sub>O<sub>3</sub>: influence of the doping ceria on the resistance toward carbon formation, *Chem. Eng. J.* 112 (1–3) (2005) 13–22.
- [5] P. Djinošić, I.G.O. Črnivec, A. Pintar, Biogas to syngas conversion without carbonaceous deposits via the dry reforming reaction using transition metal catalysts, *Catal. Today* 253 (2015) 155–162.
- [6] J. Guo, H. Lou, H. Zhao, D. Chai, X. Zheng, Dry reforming of methane over nickel catalysts supported on magnesium aluminate spinels, *Appl. Catal. A Gen.* 273 (1–2) (2004) 75–82.
- [7] M. Yu, K. Zhu, Z. Liu, H. Xiao, W. Deng, X. Zhou, Carbon dioxide reforming of methane over promoted Ni/Mg<sub>1-x</sub>O (111) platelet catalyst derived from solvothermal synthesis, *Appl. Catal. B Environ.* 148–149 (2014) 177–190.
- [8] Z. Hou, O. Yokota, T. Tanaka, T. Yashima, Characterization of Ca-promoted Ni/α-Al<sub>2</sub>O<sub>3</sub> catalyst for CH<sub>4</sub> reforming with CO<sub>2</sub>, *Appl. Catal. A Gen.* 253 (2) (2003) 381–387.
- [9] M. Sankar, N. Dimitratos, P.J. Miedziak, P.P. Wells, C.J. Kiely, G.J. Hutchings, Designing bimetallic catalysts for a green and sustainable future, *Chem. Soc. Rev.* 41 (24) (2012) 8099.
- [10] H. Wu, G. Pantaleo, V. La Parola, A.M. Venezia, X. Collard, C. Aprile, L.F. Liotta, Bi- and trimetallic Ni catalysts over Al<sub>2</sub>O<sub>3</sub> and Al<sub>2</sub>O<sub>3</sub>-MO<sub>x</sub> (M = Ce or Mg) oxides for methane dry reforming: Au and Pt additive effects, *Appl. Catal. B Environ.* 156–157 (2014) 350–361.
- [11] M.S. Fan, A.Z. Abdullah, S. Bhatia, Utilization of greenhouse gases through dry reforming: screening of nickel-based bimetallic catalysts and kinetic studies, *ChemSusChem* 4 (11) (2011) 1643–1653.
- [12] J. Zhang, H. Wang, A.K. Dalai, Development of stable bimetallic catalysts for carbon dioxide reforming of methane, *J. Catal.* 249 (2) (2007) 300–310.
- [13] J.-H. Kim, D.J. Suh, T.-J. Park, K.-L. Kim, Effect of metal particle size on coking during CO<sub>2</sub> reforming of CH<sub>4</sub> over Ni-alumina aerogel catalysts, *Appl. Catal. A Gen.* 197 (2) (2000) 191–200.
- [14] Z. Li, L. Mo, Y. Kathiraser, S. Kawi, Yolk-satellite-shell structured Ni-Yolk@Ni@SiO<sub>2</sub> nanocomposite: superb catalyst toward methane CO<sub>2</sub> reforming reaction, *ACS Catal.* 4 (5) (2014) 1526–1536.
- [15] J.W. Han, C. Kim, J.S. Park, H. Lee, Highly coke-resistant Ni nanoparticle catalysts with minimal sintering in dry reforming of methane, *ChemSusChem* 7 (2) (2014) 451–456.
- [16] E. Baktash, P. Littlewood, R. Schomäcker, A. Thomas, P.C. Stair, Alumina coated nickel nanoparticles as a highly active catalyst for dry reforming of methane, *Appl. Catal. B Environ.* 179 (2015) 122–127.
- [17] D.H. Kim, S.Y. Kim, S.W. Han, Y.K. Cho, M.-G. Jeong, E.J. Park, Y.D. Kim, The catalytic stability of TiO<sub>2</sub>-shell/Ni-core catalysts for CO<sub>2</sub> reforming of CH<sub>4</sub>, *Appl. Catal. A Gen.* 495 (2015) 184–191.
- [18] Z.-Y. Lim, C. Wu, W.G. Wang, K.-L. Choy, H. Yin, Porosity effect on ZrO<sub>2</sub> hollow shells and hydrothermal stability for catalytic steam reforming of methane, *J. Mater. Chem. A* 4 (2016) 153–159.
- [19] J.P. Dacquín, D. Sellam, C. Batiot-Dupeyrat, A. Tougerti, D. Duprez, S. Royer, Efficient and robust reforming catalyst in severe reaction conditions by nanoprecursor reduction in confined space, *ChemSusChem* 7 (2) (2014) 631–637.
- [20] S. Zhang, S. Muratsugu, N. Ishiguro, M. Tada, Ceria-doped Ni/SBA-16 catalysts for dry reforming of methane, *ACS Catal.* 3 (8) (2013) 1855–1864.
- [21] N. Wang, K. Shen, L. Huang, X. Yu, W. Qian, W. Chu, Facile route for synthesizing ordered mesoporous Ni-Ce-Al oxide materials and their catalytic performance for methane dry reforming to hydrogen and syngas, *ACS Catal.* 3 (7) (2013) 1638–1651.
- [22] Y. Wang, L. Yao, S. Wang, D. Mao, C. Hu, Low-temperature catalytic CO<sub>2</sub> dry reforming of methane on Ni-based catalysts: a review, *Fuel Process. Technol.* 169 (2018) 199–206.
- [23] Z. Bian, S. Kawi, Sandwich-like silica @ Ni @ silica multicore-shell catalyst for low temperature dry reforming of methane: confinement effect against carbon formation, *ChemCatChem* 10 (1) (2018) 320–328.
- [24] N.C. Strandwitz, G.D. Stucky, Hollow microporous cerium oxide spheres templated by colloidal silica, *Chem. Mater.* 21 (2009) 4577–4582.

- [25] G. Slowik, M. Greluk, M. Rotko, A. Machocki, Evolution of the structure of unpromoted and potassium-promoted ceria-supported nickel catalysts in the steam reforming of ethanol, *Appl. Catal. B Environ.* 221 (2018) 490–509.
- [26] Y. Du, Y. Zhu, S. Xi, P. Yang, H.O. Moser, M.B.H. Breese, A. Borgna, XAFCA: a new XAFS beamline for catalysis research, *J. Synchrotron Radiat.* 22 (2015) 839–843.
- [27] J. Ashok, M.L. Ang, P. Zhi, L. Terence, S. Kawi, Promotion of the water-gas-shift reaction by nickel hydroxyl species in partially reduced nickel-containing phyllosilicate catalysts, *ChemCatChem* 8 (2016) 1308–1318.
- [28] C. Zhang, H. Yue, Z. Huang, S. Li, G. Wu, J. Gong, Hydrogen production via steam reforming of ethanol on phyllosilicate-derived Ni/SiO<sub>2</sub>: enhanced metal–support interaction and catalytic stability, *ACS Sustain. Chem. Eng.* 1 (2013) 161–173.
- [29] J. Sehested, P.L. Hansen, S. Helveg, C. Lo, B.S. Clausen, J.R. Rostrup-nielsen, F. Abild-pedersen, Atomic-scale imaging of carbon nanofibre growth, *Nature* 427 (2004) 5–8.
- [30] G. Baure, R.M. Kasse, N.G. Rudawski, J.C. Nino, Across plane ionic conductivity of highly oriented neodymium doped ceria thin films, *Phys. Chem. Chem. Phys.* 17 (18) (2015) 12259–12264.
- [31] W. Zhang, X. Niu, L. Chen, F. Yuan, Y. Zhu, Soot combustion over nanostructured ceria with different morphologies, *Sci. Rep.* 6 (1) (2016) 29062.
- [32] J. Park, H. Lee, J. Bang, K. Park, H. Song, Chemical transformation and morphology change of nickel-silica hybrid nanostructures via nickel phyllosilicates, *Chem. Commun.* 47 (2009) 7345.
- [33] P. Burattin, M. Che, C. Louis, Characterization of the Ni (II) phase formed on silica upon deposition - precipitation, *J. Phys. Chem. B* 101 (36) (1997) 7060–7074.
- [34] B.-H. Chen, Z.-S. Chao, H. He, C. Huang, Y.-J. Liu, W.-J. Yi, X.-L. Wei, J.-F. An, Towards a full understanding of the nature of Ni(II) species and hydroxyl groups over highly siliceous HZSM-5 zeolite supported nickel catalysts prepared by a deposition-precipitation method, *R. Soc. Chem.* 45 (6) (2016) 2720–2739.
- [35] X. Kong, Y. Zhu, H. Zheng, X. Li, Y. Zhu, Y.W. Li, Ni nanoparticles inlaid nickel phyllosilicate as a metal-acid bifunctional catalyst for low-temperature hydrogenolysis reactions, *ACS Catal.* 5 (10) (2015) 5914–5920.
- [36] K. Tang, W. Liu, J. Li, J. Guo, J. Zhang, S. Wang, S. Niu, Y. Yang, The Effect of exposed facets of ceria to the nickel species in nickel-ceria catalysts and their performance in a NO + CO reaction, *ACS Appl. Mater. Interfaces* 7 (48) (2015) 26839–26849.
- [37] S. Wang, G.Q.M. Lu, Role of CeO<sub>2</sub> in Ni / CeO<sub>2</sub> ± Al<sub>2</sub>O<sub>3</sub> catalysts for carbon dioxide reforming of methane, *Appl. Catal. B Environ.* 19 (1998) 267–277.
- [38] A.J. Majewski, J. Wood, W. Bujalski, Nickel-silica core@shell catalyst for methane reforming, *Int. J. Hydrogen Energy* 38 (34) (2013) 14531–14541.
- [39] B. Nematollahi, M. Rezaei, E. Nemati, Preparation of highly active and stable NiO / CeO<sub>2</sub> 2 nanocatalysts for CO selective methanation, *Int. J. Hydrogen Energy* 40 (27) (2015) 8539–8547.
- [40] W. Zheng, J. Zhang, Q. Ge, H. Xu, W. Li, Effects of CeO<sub>2</sub> addition on Ni / Al<sub>2</sub>O<sub>3</sub> catalysts for the reaction of ammonia decomposition to hydrogen, *Appl. Catal. B Environ.* 80 (2008) 98–105.
- [41] C. Mebrahtu, S. Abate, S. Perathoner, S. Chen, G. Centi, CO<sub>2</sub> methanation over Ni catalysts based on ternary and quaternary mixed oxide: a comparison and analysis of the structure-activity relationships, *Catal. Today* 304 (2018) 181–189.
- [42] C.E. Dubé, Electrodeposition of metal alloy and mixed oxide films using a single-precursor tetranuclear copper-nickel complex, *J. Electrochem. Soc.* 142 (10) (1995) 3357.
- [43] R.B. Shalvoy, P.J. Reucroft, B.H. Davis, Characterization of coprecipitated nickel on silica methanation catalysts by X-ray photoelectron spectroscopy, *J. Catal.* 56 (3) (1979) 336–348.
- [44] D. He, H. Hao, D. Chen, J. Liu, J. Yu, J. Lu, F. Liu, G. Wan, S. He, Y. Luo, Synthesis and application of rare-earth elements (Gd, Sm, and Nd) doped ceria-based solid solutions for methyl mercaptan catalytic decomposition, *Catal. Today* 281 (2017) 559–565.
- [45] I.I. Soykal, H. Sohn, D. Singh, J.T. Miller, U.S. Ozkan, Reduction characteristics of ceria under ethanol steam reforming conditions: effect of the particle size, *ACS Catal.* 4 (2) (2014) 585–592.
- [46] T. Wu, Q. Zhang, W. Cai, P. Zhang, X. Song, Z. Sun, L. Gao, Phyllosilicate evolved hierarchical Ni- and Cu-Ni/SiO<sub>2</sub> nanocomposites for methane dry reforming catalysis, *Appl. Catal. A Gen.* 503 (2015) 94–102.
- [47] H. Ay, D. Üner, Dry reforming of methane over CeO<sub>2</sub> supported Ni, Co and Ni-Co catalysts, *Appl. Catal. B Environ.* 179 (2015) 128–138.
- [48] V.M. Gonzalez-DelaCruz, J.P. Holgado, R. Pereñíguez, A. Caballero, Morphology changes induced by strong metal-support interaction on a Ni-ceria catalytic system, *J. Catal.* 257 (2) (2008) 307–314.
- [49] T.D. Gould, M.M. Montemore, A.M. Lubers, L.D. Ellis, A.W. Weimer, J.L. Falconer, J.W. Medlin, Enhanced dry reforming of methane on Ni and Ni-Pt catalysts synthesized by atomic layer deposition, *Appl. Catal. A Gen.* 492 (2015) 107–116.
- [50] A. Kambolis, H. Matralis, A. Trovarelli, C. Papadopoulos, Ni/CeO<sub>2</sub>-ZrO<sub>2</sub> catalysts for the dry reforming of methane, *Appl. Catal. A Gen.* 377 (1–2) (2010) 16–26.
- [51] J.A. Montoya, E. Romero-Pascual, C. Gimon, P. Del Angel, A. Monzón, Methane reforming with CO<sub>2</sub> over Ni/ZrO<sub>2</sub>-CeO<sub>2</sub> catalysts prepared by sol-gel, *Catal. Today* 63 (1) (2000) 71–85.
- [52] M.-S. Fan, A.Z. Abdullah, S. Bhatia, Catalytic technology for carbon dioxide reforming of methane to synthesis gas, *ChemCatChem* 1 (2) (2009) 192–208.
- [53] L. Pino, C. Italiano, A. Vita, M. Laganà, V. Recupero, CeO<sub>2</sub>/LaO<sub>2</sub>/NiO<sub>2</sub>-δ catalyst for methane dry reforming: influence of reduction temperature on the catalytic activity and stability, *Appl. Catal. B Environ.* 218 (2017) 779–792.
- [54] W. Li, C. Liang, W. Zhou, J. Qiu, Z. Zhou, G. Sun, Q. Xin, Preparation and characterization of multiwalled carbon nanotube-supported platinum for cathode catalysts of direct methanol fuel cells, *J. Phys. Chem. B* 107 (26) (2003) 6292–6299.
- [55] Z. Li, Y. Kathiraser, S. Kawi, Facile synthesis of high surface area yolk-shell Ni@Ni embedded SiO<sub>2</sub> via Ni phyllosilicate with enhanced performance for CO<sub>2</sub> reforming of CH<sub>4</sub>, *ChemCatChem* 7 (1) (2015) 160–168.
- [56] H. Liu, D. Wierzbicki, R. Debek, M. Motak, T. Grzybek, P. Da Costa, M.E. Gálvez, La-promoted Ni-hydrotalcite-derived catalysts for dry reforming of methane at low temperatures, *Fuel* 182 (2016) 8–16.
- [57] R. Debek, M. Motak, M.E. Galvez, T. Grzybek, P. Da Costa, Promotion effect of zirconia on Mg(Ni,Al)O mixed oxides derived from hydrotalcites in CO<sub>2</sub> methane reforming, *Appl. Catal. B Environ.* 223 (2018) 36–46.
- [58] S. Yasyerli, S. Filizgok, H. Arbag, N. Yasyerli, G. Dogu, Ru incorporated Ni-MCM-41 mesoporous catalysts for dry reforming of methane: effects of Mg addition, feed composition and temperature, *Int. J. Hydrogen Energy* 36 (8) (2011) 4863–4874.
- [59] E.C. Lovell, A. Fuller, J. Scott, R. Amal, Enhancing Ni-SiO<sub>2</sub> catalysts for the carbon dioxide reforming of methane: reduction-oxidation-reduction pre-treatment, *Appl. Catal. B Environ.* 199 (2016) 155–165.
- [60] H. Arbag, S. Yasyerli, N. Yasyerli, G. Dogu, T. Dogu, Enhancement of catalytic performance of Ni based mesoporous alumina by Co incorporation in conversion of biogas to synthesis gas, *Appl. Catal. B Environ.* 198 (2016) 254–265.
- [61] L. Xu, F. Wang, M. Chen, X. Fan, H. Yang, D. Nie, L. Qi, Alkaline-promoted Co-Ni bimetal ordered mesoporous catalysts with enhanced coke-resistant performance toward CO<sub>2</sub> reforming of CH<sub>4</sub>, *J. CO<sub>2</sub> Util.* 18 (2017) 1–14.
- [62] X. Li, D. Li, H. Tian, L. Zeng, Z.J. Zhao, J. Gong, Dry reforming of methane over Ni/La<sub>2</sub>O<sub>3</sub> nanorod catalysts with stabilized Ni nanoparticles, *Appl. Catal. B Environ.* 202 (2017) 683–694.
- [63] J. Zhang, F. Li, Coke-resistant Ni@SiO<sub>2</sub> catalyst for dry reforming of methane, *Appl. Catal. B Environ.* 176–177 (2015) 513–521.
- [64] Z. Bian, I.Y. Suryawinata, S. Kawi, Highly carbon resistant multicore-shell catalyst derived from Ni-Mg phyllosilicate nanotubes@silica for dry reforming of methane, *Appl. Catal. B Environ.* 195 (2016) 1–8.
- [65] M. Yu, Y.A. Zhu, Y. Lu, G. Tong, K. Zhu, X. Zhou, The promoting role of Ag in Ni-CeO<sub>2</sub> catalyzed CH<sub>4</sub>-CO<sub>2</sub> dry reforming reaction, *Appl. Catal. B Environ.* 165 (2015) 43–56.
- [66] J.W. Han, J.S. Park, M.S. Choi, H. Lee, Uncoupling the size and support effects of Ni catalysts for dry reforming of methane, *Appl. Catal. B Environ.* 203 (2017) 625–632.
- [67] J. Deng, W. Chu, B. Wang, W. Yang, X.S. Zhao, Mesoporous Ni/Ce<sub>1-x</sub>Ni<sub>x</sub>O<sub>2-y</sub> heterostructure as an efficient catalyst for converting greenhouse gas to H<sub>2</sub> and syngas, *Catal. Sci. Technol.* 6 (3) (2016) 851–862.
- [68] K. Kamonsuangkasem, S. Therdthianwong, A. Therdthianwong, N. Thammajak, Remarkable activity and stability of Ni catalyst supported on CeO<sub>2</sub>-Al<sub>2</sub>O<sub>3</sub> via CeAlO<sub>3</sub> perovskite towards glycerol steam reforming for hydrogen production, *Appl. Catal. B Environ.* 218 (2017) 650–663.
- [69] M. Németh, Z. Schay, D. Strankó, J. Károlyi, G. Sáfrán, I. Sajó, A. Horváth, Impregnated Ni/ZrO<sub>2</sub> and Pt/ZrO<sub>2</sub> catalysts in dry reforming of methane: activity tests in excess methane and mechanistic studies with labeled <sup>13</sup>CO<sub>2</sub>, *Appl. Catal. A Gen.* 504 (2015) 608–620.
- [70] F. Pompeo, N.N. Nichio, M.G. González, M. Montes, Characterization of Ni/SiO<sub>2</sub> and Ni-Li-SiO<sub>2</sub> catalysts for methane dry reforming, *Catal. Today* 107–108 (2005) 856–862.
- [71] D. Pakhare, J. Spivey, A review of dry (CO<sub>2</sub>) reforming of methane over noble metal catalysts, *Chem. Soc. Rev.* 43 (22) (2014) 7813–7837.
- [72] P. Ferreira-Aparicio, C. Márquez-Alvarez, I. Rodríguez-Ramos, Y. Schuurman, A. Guerrero-Ruiz, C. Mirodatos, A transient kinetic study of the carbon dioxide reforming of methane over supported Ru catalysts, *J. Catal.* 184 (1) (1999) 202–212.
- [73] J. Toyir, P. Gélin, H. Belatel, A. Kaddouri, Ir/Ce<sub>0.9</sub>Gd<sub>0.1</sub>O<sub>2-x</sub> as a new potential anode component in solid oxide fuel cells integrating the concept of gradual internal reforming of methane, *Catal. Today* 157 (1–4) (2010) 451–455.
- [74] P. Ferreira-Aparicio, I. Rodríguez-Ramos, J. Anderson, A. Guerrero-Ruiz, Mechanistic aspects of the dry reforming of methane over ruthenium catalysts, *Appl. Catal. A Gen.* 202 (2) (2000) 183–196.
- [75] M.A. Vasiliades, M.M. Makri, P. Djinojić, B. Erjavec, A. Pintar, A.M. Efstathiou, Dry reforming of methane over 5 wt% Ni/Ce<sub>1-x</sub>Pr<sub>x</sub>O<sub>2</sub>-δ catalysts: performance and characterisation of active and inactive carbon by transient isotopic techniques, *Appl. Catal. B Environ.* 197 (2016) 168–183.
- [76] P. Fornasiero, G. Balducci, R. Di Monte, J. Kašpar, V. Sergio, G. Gubitosa, A. Ferrero, M. Graziani, Modification of the redox behaviour of CeO<sub>2</sub> induced by structural doping with ZrO<sub>2</sub>, *J. Catal.* 164 (1) (1996) 173–183.
- [77] J.M. Ginsburg, J. Piña, T. El Solh, H.I. De Lasa, Coke formation over a nickel catalyst under methane dry reforming conditions: thermodynamic and kinetic models, *Ind. Eng. Chem. Res.* 44 (14) (2005) 4846–4854.